SLIP FREQUENCY PHASE LOCK LOOP (PLL) FOR DECOUPLED P-Q CONTROL OF DOUBLY-FED INDUCTION GENERATOR (DFIG)

Baike Shen

B.Eng. Tsinghua University, P.R.China

A thesis submitted to
The Faculty of Graduate Studies and Research
In partial fulfillment of the requirements for the degree of
Master of Engineering

Department of Electrical and Computer Engineering McGill University Montreal, Quebec, Canada

October 2004

© Baike Shen, 2004



Library and Archives Canada

Published Heritage Branch

395 Wellington Street Ottawa ON K1A 0N4 Canada Bibliothèque et Archives Canada

Direction du Patrimoine de l'édition

395, rue Wellington Ottawa ON K1A 0N4 Canada

> Your file Votre référence ISBN: 0-494-06585-0 Our file Notre référence ISBN: 0-494-06585-0

NOTICE:

The author has granted a nonexclusive license allowing Library and Archives Canada to reproduce, publish, archive, preserve, conserve, communicate to the public by telecommunication or on the Internet, loan, distribute and sell theses worldwide, for commercial or noncommercial purposes, in microform, paper, electronic and/or any other formats.

AVIS:

L'auteur a accordé une licence non exclusive permettant à la Bibliothèque et Archives Canada de reproduire, publier, archiver, sauvegarder, conserver, transmettre au public par télécommunication ou par l'Internet, prêter, distribuer et vendre des thèses partout dans le monde, à des fins commerciales ou autres, sur support microforme, papier, électronique et/ou autres formats.

The author retains copyright ownership and moral rights in this thesis. Neither the thesis nor substantial extracts from it may be printed or otherwise reproduced without the author's permission.

L'auteur conserve la propriété du droit d'auteur et des droits moraux qui protège cette thèse. Ni la thèse ni des extraits substantiels de celle-ci ne doivent être imprimés ou autrement reproduits sans son autorisation.

In compliance with the Canadian Privacy Act some supporting forms may have been removed from this thesis.

While these forms may be included in the document page count, their removal does not represent any loss of content from the thesis.

Conformément à la loi canadienne sur la protection de la vie privée, quelques formulaires secondaires ont été enlevés de cette thèse.

Bien que ces formulaires aient inclus dans la pagination, il n'y aura aucun contenu manquant.



Dedicated to my wife and my son

ABSTRACT

The term "sensor-less" in power electronic drives refers to measurement of mechanical shaft position and/or speed from the currents and voltages of the electrical machine. This thesis presents innovative sensor-less means (a Slip Frequency Phase Lock Loop (PLL) and a γ - δ Axes Aligner) for implementing decoupled P-Q control of a doubly-fed induction generator (DFIG) for wind-turbine application. Proofs of concepts are by digital simulations.

The accuracy of the Slip Frequency Phase Lock Loop in speed estimation is evaluated; the origin of a shortcoming (small phase lag) located and compensated for.

The Slip Frequency Phase Lock Loop (PLL) and a γ - δ Axes Aligner are then evaluated as parts of the decoupled P-Q control of a wind turbine driven doubly-ed induction generator. The research succeeds in realizing robust decoupled P-Q control, that is one in which the generator parameters do not have to be known precisely and can have minor variations such as drifts with temperature. The system has been successfully tested for optimal wind power acquisition.

RÉSUMÉ

Ce mémoire propose un algorithme de commande découplée de la puissance active et réactive (P-Q) pour une machine asynchrone à double alimentation. Cet algorithme a la particularité qu'il n'utilise pas les mesures de position et de vitesse de l'arbre de la machine. En lieu de ces mesures mécaniques, il utilise les mesures des courants et tensions de la machine.

L'algorithme fonctionne à l'aide d'une boucle à verrouillage de phase de la fréquence de glissement et d'un mécanisme d'alignement d'axe γ - δ . L'algorithme est destiné notamment à la commande de la puissance active et réactive d'un ensemble éolienne-alternateur asynchrone à double alimentation. L'approche est validée à l'aide de simulations numériques.

La précision de la boucle à verrouillage de phase de la fréquence de glissement comme mécanisme d'estimation de la vitesse de rotation de la machine est évaluée. L'origine d'une erreur d'estimation, un certain retard de phase, est identifiée et compensée.

La boucle à verrouillage de phase de la fréquence de glissement et le mécanisme d'alignement d'axe γ - δ sont évalués séparément. On démontre que l'algorithme de commande est robuste, car la connaissance exacte des paramètres constitutifs de la machine électrique n'est pas nécessaire au bon fonctionnement de celui-ci. Donc, des variations mineures de température ou des conditions de vent n'ont pas d'effet sur la performance de l'algorithme. On démontre enfin que l'algorithme de commande permet au couple éolienne-alternateur d'optimiser la conversion d'énergie en fonction de la vitesse du vent.

ACKNOWLEDGEMENTS

My sincere thanks go to Prof. Dr. B.T.Ooi, my supervisor, for his extremely helpful guidance, continuous encouragement, inspiration, generous support and friendship that guide me through the research work.

I am very thankful to Professor Dr. G. Joos and Professor F.D. Galiana for letting me have full access to computer equipment and simulation software that greatly facilitated the research.

I am grateful to Mr.Chad Abbey, for his work in correcting my English, for his precious comments, for his friendly help. I appreciate Dr. Lianwei Jiao, for his technical assistance. I thank Mr. Francois Bouffard, for translating the abstract of this thesis to French, and for his friendship.

I also want to thank Dr. Banakar, Dr. Fawzi A. Rahman Al-Jowder, Mr. Yongjun Ren, Ms. Jing Wang, Mr. Fengquan Zhou, Mr.Wei Li, Mr. Changlin Luo, Mr.Alaa Abdul Samad, Mr. Victor Low and Mr. Ming Zou.

I would like to extend my thanks to Mr. Carl Jorgensen, Mr. Joseph Mui, Mr. Charless Basseha for helping me deal with some computer and software related technical problems. I would like to thank the secretaries of the Department of Electrical and Computer Engineering, for their unstinting help whenever I asked for it.

The research is sponsored by the Natural Science and Engineering Research Council (NSERC) of Canadian through a Strategic Grant on "Integrating distributed energy sources into the electric power grid".

I must give special thanks to my wife, Kuihua and my son, Yichen. Without their everlasting love, I would never have been able to finish my M.Eng. study. My special thanks also go to my Mother for her encouragement and support.

TABLE OF CONTENTS

ABSTRACT	i
RÉSUMÉ	ii
ACKNOWLEDGMENTS	iii
TABLE OF CONTENTS	iv
LIST OF FIGURES	vii
LIST OF ACRONYMS	X
LIST OF MAIN SYMBOLS	xi
Chapter 1 Introduction	1
1.0 Overview	1
1.0.1 Renewable Energy Research in Canada	1
1.1 Objectives of Thesis	3
1.2 Research Tools	4
1.3 Organization of Thesis	5
Chapter 2 Slip Frequency Phase Lock Loop and New γ-δ Ax	es Aligner
for DFIG	7
2.0 Introduction	7
2.1 Traditional Three-Phase Lock Loop (PLL)	8
2.2 Slip Frequency Phase Lock Loop (PLL)	11
2.2.1 Phase Mixer	11
2.2.2 Phase Detector	11
2.2.3 Speed Estimation	12
2.3 Proof of Concept of Slip Frequency PLL	12
2.4 α-β to γ-δ Transformation	14
2.4.1 Stator Voltage Transformation	12
2.4.2 Rotor Current Transformation	13
2.4.3 γ-δ Axes Aligner	15
2.4.4 Proof of Concept γ-δ Axes Aligner	17
2.4.5 Influence of error in R_S , L_{lS} and L_m on Estimated Rotor Position	17
2.4.5.1 Case Study—Parameter Sensitivity $-R_S$	18
2.4.5.1 Case Study—Farameter Sensitivity $-K_S$ 2.4.5.2 Case Study—Parameter Sensitivity $-L_{lS}$ and L_m	19
2.4.5.2 Case Study—I arameter Sensitivity $-L_{is}$ and L_{m} 2.5 Explanation for Robustness	19
2.6 Conclusion	21
Chapter 3 Speed Estimation by Slip Frequency	
Phase Lock Loop (PLL)	23

3.0 Introduction	23
3.1 Calibrating Slip Frequency Phase Lock Loop (PLL)	24
3.2 Frequency Domain Evaluation of Slip Frequency PLL	25
3.3 Analytical Model of Slip Frequency PLL	28
3.3.1 Linearized Model of Slip Frequency Lock Loop	28
3.3.1.1 Transfer Function of Phase Detector	30
3.3.1.2 Close Loop Transfer Function of Linearized Slip Frequency PLL	30
3.3.1.3 Transfer Function of P-I Block	30
3.3.1.4 Transfer Function of Linearized Slip Frequency PLL	31
3.3.1.5 Parameters Design	31
3.3.2 Phase Shift Caused by Time Delay in Current Measurement	33
3.4 Speed Estimation of DFIG Connected to	22
Voltage-Source Converter(VSC)	34
3.4.1 Lead-lag Block Design	36
3.5 Conclusion	37
3.5 Conclusion	51
Chantan A. Cangawlegg Dagawaled D. O. Cantual for DEIC	39
Chapter 4 Sensorless Decoupled P-Q Control for DFIG	39
4.0 Introduction	39
4.1 Doubly-fed Induction Generator Model	40
4.1.1 Stationary and Rotating Coordinate	40
4.1.2 Circuit Model of a Three-Phase Induction Machine	42
4.1.3 Machine Model in γ-δ-0 Reference Frame	43
4.2 Wind Turbine Model	46
4.3 Control of Rotor Side Converter(VSC)	48
4.3.1 Slip Frequency PLL and γ-δ Axes Aligner Block	49
4.3.2 P_s and Q_s Reference Generator Block	50
4.3.3 P_s and Q_s Computation Block	51
4.3.4 Negative Feedback of Complex Power	51
4.3.5 Rotor Voltage and Current Control Block	51
4.4 Control of Front End Converter (Stator Side Converter)	52
4.4.1 Hysteresis Current Control	53
4.4.2 DC Voltage Regulator	56
4.4.3 Simulation result of DC Voltage Regulator	57
4.5 Simulation Tests on DFIG	59
4.5.1 Static simulation tests of Sensor-less decoupled P-Q control	60
4.5.2 Test on Robustness	61
4.5.2.1 Stator Resistor Uncertainty R_S	61
4.5.2.2 Stator Leakage Inductance Uncertainty- L_{lS}	62
4.5.2.3 Magnetizing Inductance Uncertainty $-L_m$	63
4.5.2.4 Basis of Robustness	64
4.5.3 Dynamic Tests	65
4.5.3.1 Dynamic Test of Slip Frequency PLL and γ-δ Axes Aligner	65
4.5.3.2 Dynamic Tests on Robustness	67
4.6 CONCLUSIONS	68

LIST OF FIGURES

Chapter 1

Fig. 1-1 System Configuration of Doubly-Fed Induction Generator	2
Chapter 2	
Fig. 2.1 Street, and of the distance where Dhare I and I am	0
Fig. 2-1 Structure of tradition three-phase Phase Lock Loop	10
Fig. 2-2 (a) Schematic of Slip Frequency PLL Fig. 2-2 (b) Phase Mixer	10 10
Fig. 2-2 (b) Phase Mixer Fig. 2-3 Proof of Slip Frequency PLL	13
Fig. 2-4 γ - δ and γ *- δ * axes frame separated by ϕ	15
Fig. 2-4 γ-6 and γ'-6' axes frame separated by φ Fig. 2-5 Block Diagram of γ-δ Axes Aligner	16
· · · · · · · · · · · · · · · · · · ·	
Fig. 2-6 Proof of γ-δ Axes Aligner Fig. 2-7 (a) Simulated waveforms of estimated and estual rates position P. =0	17 18
Fig. 2-7 (a) Simulated waveforms of estimated and actual rotor position $R_S=0$ Fig. 2-7 (b) Simulated waveforms of estimated and actual rotor position	10
$R_{\rm S}$ =2 X actual value (0.0062 p.u.)	18
Fig. 2-8 (a) Simulated waveforms of estimated and actual rotor position $L_{IS}=0$	
Fig. 2-8 (b) Simulated waveforms of estimated and actual rotor position	20
$L_{\rm IS}$ =2 X actual value (0.0086 p.u.)	20
Fig. 2-9 (a) Simulated waveforms of estimated and actual rotor position	
Lm=0.5 X actual value	20
Fig. 2-9 (b) Simulated waveforms of estimated and actual rotor position	
$L_{\rm m}$ =2 X actual value	20
Chapter 3	
Fig. 3-1 Configuration of Induction Machine System	25
Fig. 3-2 Torque Control Block Diagram	25
Fig. 3-3 (a) Estimated Speed and Actual Speed under f=1Hz	26
Fig. 3-3 (b) Estimated Speed and Actual Speed under f = 2Hz	26
Fig. 3-3 (c) Estimated Speed and Actual Speed under f=3Hz	27
Fig. 3-3 (d) Estimated Speed and Actual Speed under f =4Hz	27
Fig. 3-3 (e) Estimated Speed and Actual Speed under f=5Hz	27
Fig. 3-3 (f) Estimated Speed and Actual Speed under f=10Hz	27
Fig. 3-3 (d) Estimated Speed and Actual Speed under f=15Hz	28
Fig. 3.4 Phase Difference between Estimated Speed and Actual Speed	
28	•
Fig. 3.5 Structure of VCO	29
Fig. 3.6 Linearized Model of Slip Frequency PLL	30
Fig. 3.7 Bode diagram of transfer function of linearized Slip Frequency PLL	32

LIST OF FIGURES

	Fig. 3.8 Phase Difference between Estimated Speed and Actual Speed	
	for DFIG	34
	Fig. 3.9 FFT of Rotor Current	35
	Fig. 3.10 Estimated Speed by Using Butterworth Filter	36
	Fig. 3.11 Estimating Rotor Speed Diagram	36
	Fig. 3.12 Estimated Speed after passing through lead-lag block	37
Chapt	ter 4	
	Fig. 4.1 Relationship between α - β and γ - δ frames	41
		47
	Fig. 4.3 Wind Power-vs- Rotor Speed	48
	Fig. 4.4 Block Diagram of Rotor side VSC Control	49
	Fig. 4.5 (a) P_S Reference Generator	50
	Fig. 4.5 (b) T_{mech} Generator	50
	Fig. 4.6 Single Phase Hysteresis Current Controlled Converter	53
	Fig. 4.7 $i_a(t)$ Tracking Current $i_R(t)$ Within the tolerance band h	54
	Fig. 4.8 3-Phase Converter with Inner Hysteresis Current Loop and Outer Volta	
	Regulator Loop Fig. 4.0 (a) DC Valtage Control of Out Loop (Phage Current Congretor)	55 57
	Fig. 4.9 (a) DC Voltage Control of Out-Loop (Phase-Current Generator)	57 57
	Fig. 4.9 (b) Q Control of Outer-Loop (Phase-Current Generator)	57
	Fig. 4.9 (c) Current Transformation From $\gamma - \delta$ Frame to a-b-c Frame	31
	Fig. 4.10 (a) Vdc when Step change of V_{dc}^* from 1500 V to 0 V at t=1000ms 58	
	Fig. 4.10 (b) P_{con} and Q_{con} When step change of V_{dc}^* from 1500 V to 0 V	
	at 1000ms	58
	Fig. 4.11 (a) Slip s when DFIG running from sub-synchronous speed to super-	50
	J I	59
	Fig. 4.11 (b) P_{con} when DFIG running from sub-synchronous speed to super-	
	7 1	59
	Fig. 4.11 (c) V_{dc} when DFIG running from sub-synchronous speed to super-	
	synchronous speed	59
		60
		60
		62
	Estrated in Estate State	62
	Fig. 4.14 (a) Q_{sref} and Measured Q_s : Q_{serf} Variable,	(2
	- 3, cy 1	63
	Fig. 4.14 (b) P_{sref} and Measured P_s : Q_{serf} Variable,	62
	P_{sref} =constant, L_{lS} =0.172 p.u.	63
	Fig. 4.15 (a) Q_{sref} and Measured Q_s : Q_{serf} Variable,	65
	P_{sref} =constant, L_m =1.55 p.u.	65

LIST OF FIGURES

Fig. 4.15 (b) P_{sref} and Measured P_s : Q_{serf} Variable,	
P_{sref} =constant, L_m =1.55 p.u.	65
Fig. 4.16 (a) Wind Velocity: Variable wind Speed Q_{sref} =constant	66
Fig. 4.16 (b) Rotor Speed: Variable wind Speed Q_{sref} =constant	66
Fig. 4.16 (c) P_{sref} and Measured P_s : Variable wind Speed Q_{sref} =constant	66
Fig. 4.16 (d) Q_{sref} and Measured Q_s : Variable wind Speed Q_{sref} =constant	66
Fig. 4.17 (a) P_{sref} and Measured P_s : Variable wind Speed Q_{sref} =constant,	
$R_S = 0, L_{IS} = 0, L_m = 1.55 \text{ p.u.}$	67
Fig. 4.17 (b) Q_{sref} and Measured Q_s : Variable wind Speed Q_{sref} =constant	
$R_S = 0, L_{lS} = 0, L_m = 1.55 \text{ p.u.}$	67

LIST OF ACRONYMS

AC/ac Alternating Current
DC/dc Direct Current

DFIG Doubly-Fed Induction Generator EMTP Electromagnetic Transient Program

FEC Front-End Converter
FFT Fast Fourier Transform
HVDC High Voltage Direct Current
IGBT Isolated Gate Bipolar Transistor

PI Proportional and Integral
PLL Phase Locked Loop
PWM Pulse Width Modulation

SPWM Sinusoidal Pulse Width Modulation

SRIM Slip Ring Wound Rotor Induction Machine

VCO Voltage Controlled Oscillator VSC Voltage Source Converter

LIST OF MAIN SYMBOLS

ϕ	Output Angle of γ-δ Aligner
$\overset{r}{ heta}$	Output of Slip Frequency PLL
ω	Angular frequency of a signal
ω_0	Central frequency of PLL
ω_{s}	Grid angular frequency
_	Actual speed of the rotor in mechanical
ω_m	Rotor side angular frequency
ω_R	
ω_{est}	Estimated value of rotor speed
ω_X	Angular frequency of the output signal of VCO Power coefficient of the wind turbine
C_p	
$u_{con_a} u_{con_b}, u_{con_c}$	Three-Phase converter voltages
u_{sa}, u_{sb}, u_{sc}	Three-Phase stator voltages
u_{ra}, u_{rb}, u_{rc}	Three-Phase rotor voltages
u_{dc}	DC-link Voltage
$u_{con_\chi}u_{con_\delta}$	Components of converter voltage in stator γ-δ frame
$u_{s\alpha}u_{s\beta}$	Components of stator voltage in stator α - β frame
$u_{s\gamma}, u_{s\delta}$	Components of stator voltage in stator γ - δ frame
$u_{r\alpha}u_{r\beta}$	Components of rotor voltage in stator α - β frame
$u_{r\gamma}, u_{r\delta}$	Components of rotor voltage in stator γ-δ frame
$i_{con_a}, i_{con_b}, i_{con_c}$	Three-phase converter current
i_{sa}, i_{sb}, i_{sc}	Three-Phase stator current
i_{ra}, i_{rb}, i_{rc}	Three-Phase rotor current
$i_{s\alpha}, i_{s\beta}$	Components of stator current in stator α - β frame
$i_{sp}i_{s\delta}$	Components of stator current in stator γ - δ frame
$i_{r\alpha}i_{r\beta}$	Components of rotor current in stator α - β frame
$i_{rj},i_{r\delta}$	Components of rotor current in stator γ-δ frame
i_{ms}	Magnetizing current
J	Mechanical load inertia
h	Tolerance band
δ	Initial angle of corresponding variables
ρ	Air density
p	Number of poles
P	Real power
P_S	Stator side real power
P_t	Real power produced by wind turbine
P_{con}	Real power passing through converter
Q	Reactive power
Qs	Stator side reactive power Reactive power passing through converter
Q_{con}	Reactive power passing inrough converter

LIST OF MAIN SYMBOLS

Superscript denoting refence values of corresponding variables

r	Turbine rotor radius
S	Rotor slip
S_a	Switch function for Phase-a
ε	Error of corresponding variables
L_m, L_S, L_R	Magnetising, Stator and rotor inductances
L_{ls} , L_{lR}	Stator and rotor leakage inductances
R_S, R_R	Stator and rotor resistances
T_S , T_R	Stator and rotor time constants
T_{damp}	Damping torque
T_m	Mechanical torque
T_e	Electromagnetic torque
V_w	Wind Velocity
S: Stator	R: Rotor
m: rotor shaft	ref: Reference
con: Converter	•

Introduction

1.0 Overview

Even though harnessing power from wind can be traced back to approximately 4000 years, there has been a renewed interest in the subject in recent years. This is because wind energy, as with other renewable energy sources, meets the Kyoto Protocol requirement of being free of Green House Gas Emissions—CO₂, nitrous oxide and methane [1]. With the development of aerodynamic designs, wind turbines that can capture a few megawatts of power are available [2].

1.0.1 Renewable Energy Research in Canadian Universities

Literature search shows that only a few universities in Canada are involved in research on wind and renewable resource: the University of New Brunswick has an NSERC Chair in Environmental Design Engineering (Dr. Liuchen Chang, on wind and solar energy for agro-business and remote communities); Dalhousie University has "Nova Scotia Energy Project" to demonstrate how wind energy could be used to mitigate climate change (Dr. Larry Hughes and Dr. Tim Little); the University of Quebec at Rimouski has researched on wind energy assessment (Dr. Jean-Louis Chaumel). As wind energy research has been active only in recent years, it is possible that many groups have been left out because of publication delays.

Wind Energy Research in McGill University

In the late 1960s, funded by the Brace Research Institute, McGill University researched on wind power for pumping potable water in remote communities. Professor Joos, then a graduate student, simulated a wind turbine drive for a laboratory test of a wind generator. In the early 1970s when the OPEC nations raised the price of energy, the

Société québécoise d'exploration minière (SOQUEM) contracted McGill University to do a feasibility study on energizing a salt mining operation on the Magdalen Islands with wind power.

At that time, the existing knowledge on wind power in North America was summarized by P.C. Putnam, in his book *Power From the Wind* [3]. The lessons learned from this contract were: wind power was of low density—requiring aggregation and of low reliability—requiring storage. Although research on wind energy per se was put on a back burner when the price of energy dropped, McGill University continued research on induction generators [4] and power electronic controllers of interfaces [5]. After a lapse of almost three decades, on returning to research on wind energy, it is found that the doubly-fed induction generator is a contender in the choice of wind generators.

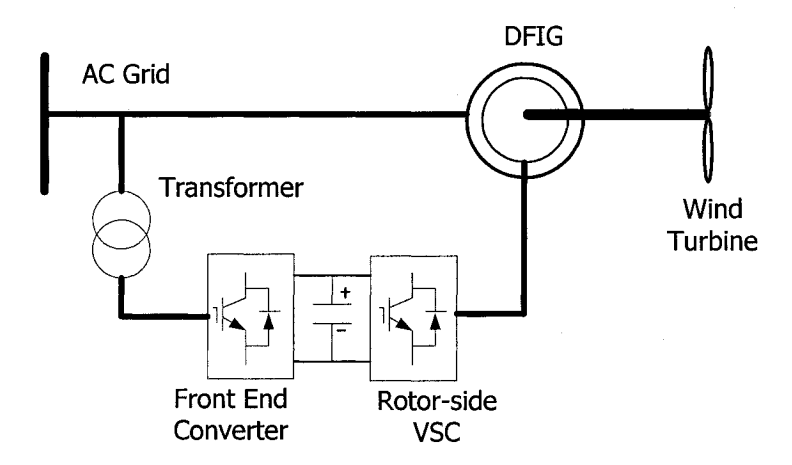


Fig.1-1 System Configuration of Doubly-Fed Induction Generator

The doubly-fed induction generator (DFIG) is an excellent choice as a wind generator because its stator can be connected directly to the 60 HZ ac grid even though the rotor speed ω_m can be change with the prevailing wind velocity V_w . The real power P_s and the reactive power Q_s from the stator side can be controlled at the rotor side by a Voltage-Source Converter (VSC) connected to the slip-ring terminals. As shown in Fig.1-1, the rotor-side VSC is connected back-to-back on its dc side to a second VSC (Front End Converter) which conveys the rotor slip frequency power to 60 Hz power of the utility grid. A transformer is usually needed to step up the low voltages of the VSC to ac grid voltages. The advantage of rotor-side control comes from the lower kVA rating of the

VSCs. The reduction is by a factor of the maximum operating slip s_{max} (usually $|s| \le 0.3$).

Research in DFIG

The economic and technical advantages of the DFIG and the promise of wide applications in wind turbines have stimulated research [6-9] which combine sensorless schemes together with field orientated control. The objective of field orientated control is to achieve decoupled P-Q control.

As we know, decoupled control of the real power P_s and the reactive power Q_s of the DFIG requires the dynamic equations to be formulated in the synchronously rotating $\gamma - \delta$ reference frame. An absolute position encoder, which measures the rotor position, facilitates the erection of $\gamma - \delta$ reference frame which is common to both the stator-side and the rotor-side voltages [10]. The rotor speed ω_m is obtained by differentiating the position from the encoder.

As absolute position encoders are expensive, sensorless schemes [6,8,9] are preferred. Sensorless schemes are based on the measurements of the stator and the rotor currents from which the position of the airgap magnetizing flux axis is estimated and thereafter the position of the $\gamma - \delta$ axes is inferred. L. Morel, H. Godfroid, A. Mirzaian and J.M. Kauffmann [8] were the earliest pioneers to propose rotor position sensing in the DFIG. The rotor speed ω_m is then obtained by differentiating the rotor position. Since differentiation is inherently a noisy operation and the rotor currents contain the harmonics of the Voltages-Source Converter (VSC) operated by PWM switching, errors in the rotor speed ω_m estimation are to be expected.

1.1 Objectives Of Thesis

From the work of previous researchers [6-9], the following weaknesses are noted in existing designs:

- (1) the estimated rotor speed is noisy because the information is obtained by differentiating the estimated rotor position. Differentiation is inherently noisy.
- (2) the estimated rotor position is itself noisy because it is based on the measurements of the rotor currents which contain switching harmonics of the VSC.
- (3) the estimated rotor position method relies on having accurate information regarding the parameters of the DFIG.
- (4) the decoupled P-Q control method relies on having accurate information regarding the parameters of the DFIG.

Therefore, it is desirable to have a decoupled P-Q control which is: (i) more accurate in speed measurement and (ii) robust and less sensitive to parameter variation.

This thesis presents an alternative sensorless scheme based on:

- An innovative Slip Frequency Phase Lock Loop which directly measures the rotor frequency ω_r and the rotor speed ω_m of the doubly-fed induction generator (DFIG).
- A new $\gamma \delta$ Axes Aligner.

As the alternative sensorless scheme (Slip Frequency Phase Lock Loop and $\gamma - \delta$ Axes Aligner) is just invented and reported in this thesis, proofs of concepts, at this early stage, are entirely by simulations. Simulations proofs of the sensorless scheme which enable decoupled P-Q control to be implemented at the rotor terminals of a DFIG are given.

1.2 Research Tools

The sensorless decoupled P-Q control of a DFIG model has been evaluated using digital simulations. The simulation software is EMTP(R). EMTP(R) is a revised version of Professor Dommel's Electromagnetic Transient Program and is being developed by Hydro-Quebec for power system planning. EMTP(R) has many features for incorporating

power electronic controllers and includes a software model of the wound rotor induction machine which is conveniently used to represent the DFIG.

1.3 Organization of Thesis

This thesis is organized as follows:

- *Chapter 1*: Introduction.
- Chapter 2: Slip Frequency Phase Lock Loop and new γ δ Axes Aligner for DFIG.
- *Chapter 3*: Speed estimation by using Slip Frequency Phase Lock Loop.
- Chapter 4: Sensorless Decoupled P-Q Control for DFIG.
- Chapter 5: Conclusions and future work

Chapter 1: Chapter 1 introduces the development and advantage of DFIG in wind farms and gives a brief description of the research on the sensorless decoupled P-Q control of the DFIG.

Chapter 2: Chapter 2 describes the novel Slip Frequency Phase Lock Loop that is adapted from a traditional Phase Lock Loop (PLL). The chapter proposes a new $\gamma - \delta$ Axes Aligner. $\gamma - \delta$ axes alignment is required to implement decoupled P-Q control at the rotor side.

Chapter 3: Chapter 3 evaluates the accuracy of the speed estimation by the novel Slip Frequency Phase Lock Loop. A mathematical model of Slip Frequency Phase Lock Loop has been constructed to pinpoint the source of inaccuracy, which appears as a phase shift. It is found that the inaccuracy comes from the electrical time constants of the DFIG and not from the Slip Frequency Phase Lock Loop. A phase shift compensation method is proposed and its adequacy is demonstrated by simulations.

Chapter 4: Chapter 4 presents mathematical models which have been used in the simulations of the thesis: model of the DFIG, model of the wind turbine, and the phase shift compensation method of chapter 3. They are incorporated incorporated into simulation models of the Slip Frequency Phase Lock Loop and the $\gamma - \delta$ Axes Aligner of chapter 2.

The sensorless, decoupled P-Q control of the DFIG as driven by a wind-turbine is simulated. It is shown that the Current Tracking Control enables decoupled P-Q control to be implemented without requiring accurate knowledge of the parameters of the DFIG.

Chapter 5: The conclusions of the study are presented and the suggestions for future work are given.

Chapter 2

Slip Frequency Phase Lock Loop and New $\gamma - \delta$ Axes Aligner for DFIG

2.0 Introduction

The alternate sensorless decoupled P-Q control for the DFIG of this thesis does not depend on differentiating the rotor position with respect to time to obtain the rotor speed. It is based on measuring the rotor slip frequency ω_r . The measurement of the rotor frequency ω_r is accomplished by a Slip Frequency Phase Lock Loop (PLL). Then the rotor speed in electrical radians/s is obtained from the equation $\omega_m = \omega_s - \omega_r$.

The Slip Frequency PLL, has been adapted from the PLL in Mr. Jian Hu's McGill University Master thesis [11]. This PLL has been shown to be capable of: (1) excellent phase tracking, (2) broad range acquisition, (3) very good immunity against high frequency noise. The adaptation is necessary because as the rotor speed passes from subsynchronous ($\omega_m < \omega_s$) to super-synchronous ($\omega_m > \omega_s$) speed, the rotor frequency $\omega_r = \omega_s - \omega_m$ passes from positive frequency through zero to negative frequency. As it is not clear how the phase detector and the Voltage Controlled Oscillator (VCO) in the conventional PLL will handle positive, zero and negative frequencies, the Slip Frequency PLL is proposed.

The Slip Frequency PLL sidesteps the difficulties by letting the Voltage Controlled Oscillator (VCO) generate a frequency ω_x , treated as an algebraic unknown, which is added to the frequency ω_r of the rotor currents. The VCO of the Slip Frequency PLL is then made to track the stator frequency ω_s . The phase detector compares the sum $(\omega_r + \omega_x)$ with the stator frequency ω_s and applies the error to the input of the VCO in negative feed back. As the PLL applies $\omega_r + \omega_x$ to track the stator frequency ω_s , the output frequency ω_s of the VCO is always positive. Furthermore, the detector does not have to deal with zero or negative frequency.

On successful locking to the stator frequency, one has the equality $(\omega_r + \omega_x) = \omega_s$. Since one also has the relationship $(\omega_r + \omega_m) = \omega_s$ from induction machine theory, it follows that the frequency output of the VCO is the measurement of the rotor speed, i.e. $\omega_x = \omega_m$ and furthermore the rotor frequency $\omega_r = \omega_s - \omega_x$.

From the Slip frequency PLL, one has the angular frequency $(\omega_r + \omega_x)$ which is the speed at which the $\gamma^* - \delta^*$ axes of the rotor currents rotate. Unfortunately, this rotor current $\gamma^* - \delta^*$ axes is not the $\gamma - \delta$ axes of the stator voltages which is required for the decoupled P-Q control of DFIG. A new $\gamma - \delta$ Axes Aligner is then proposed. It applies negative feedback to determine the angle Φ by which the $\gamma^* - \delta^*$ axes of the rotor currents must be rotated in order to locate the stator voltage $\gamma - \delta$ axes.

The information extracted by the Slip Frequency PLL are: (i) the rotor speed ω_m , (ii) the rotor frequency ω_r .

The information extracted by the $\gamma - \delta$ Axes Aligner is the position of the $\gamma - \delta$ frame at which decoupled P-Q control can be implemented by the rotor-side VSC.

2.1 Traditional Three-Phase Lock Loop (PLL)

For completeness, it is first necessary to present the traditional three-phase PLL which is illustrated in Fig.2-1 [11]. In the single phase PLL, there is the double frequency component after the detection stage which has to be filtered out. The double-frequency term is automatically cancelled out in the three-phase or two-phase PLL. This is important in power system application because the double frequency term is 120Hz and the filter will be costly for such low frequency.

The first stage of three-phase PLL has a transformation from the a-b-c frame to the α - β -0 frame using the equations:

$$\begin{vmatrix} x_{\alpha} \\ x_{\beta} \\ x_{0} \end{vmatrix} = \frac{2}{3} \begin{vmatrix} 1 & -\frac{1}{2} & -\frac{1}{2} \\ 0 & -\frac{\sqrt{3}}{2} & \frac{\sqrt{3}}{2} \\ \frac{1}{2} & \frac{1}{2} & \frac{1}{2} \end{vmatrix} \begin{vmatrix} x_{a} \\ x_{b} \\ x_{c} \end{vmatrix}$$
 (2.1)

where x_a, x_b and x_c (e.g. stator side voltage or rotor side current) are three-phase quantities in the a-b-c frame.

 x_{α} , x_{β} and x_{0} are three-phase quantities in the α - β -0 frame.

The Phase Lock Loop consists of a phase detector, a P-I block and a block of gain K_{ν} , which relates the input signal U_f to the output frequency through the equation $d\omega = K_{\nu}U_f$. The central frequency of PLL ω_0 is added so that $\omega = \omega_0 + d\omega$ to improve the overall tracking performance of the PLL. After the 1/s block which relates angular frequency ω to angle θ are two function generators $\sin()$ and $\cos()$. The Phase Detector in nulling the error $\varepsilon_u = v_{c\alpha} \cos \theta - v_{c\beta} \sin \theta$ locks the phase θ of the PLL to the phase angle of the α - β frame signals. As reported in [11], the Phase Lock Loop has excellent phase tracking performance with broad frequency acquisition range and good immunity against high frequency noise.

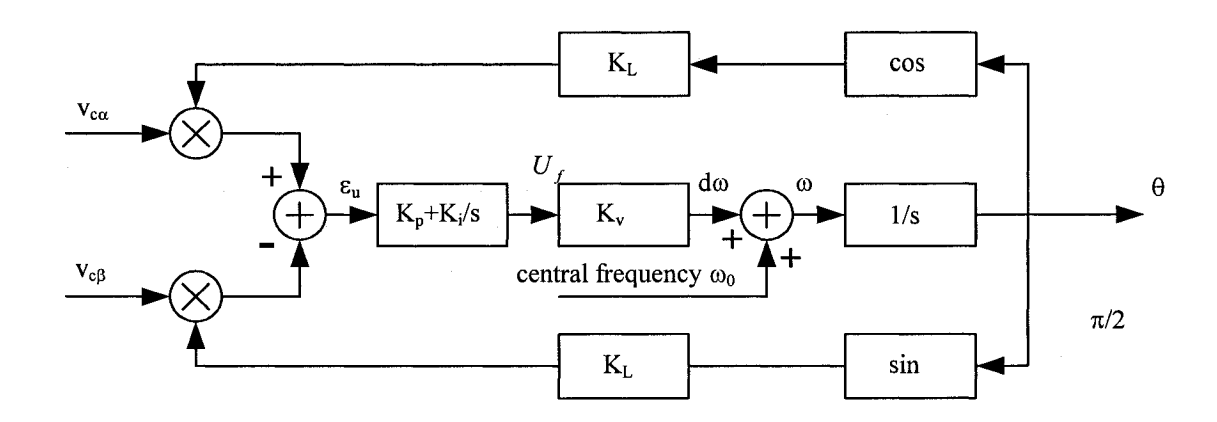
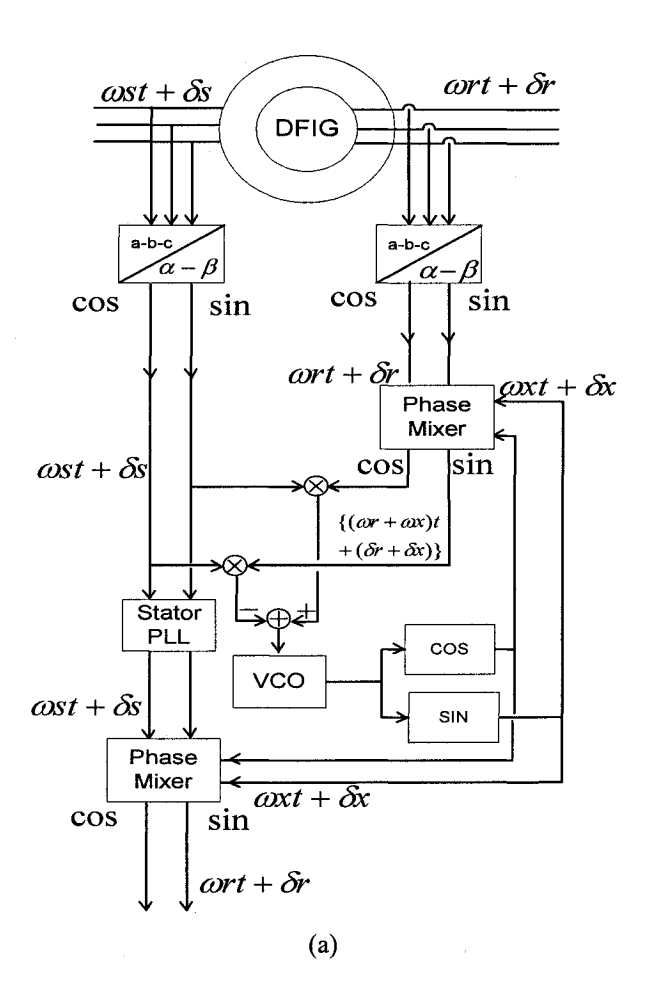


Fig. 2-1 Structure of traditional three-phase Phase Lock Loop



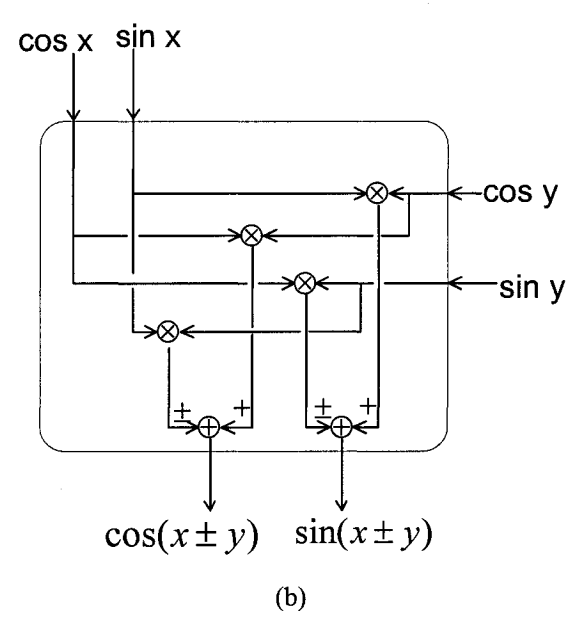


Fig.2-2 (a) Schematic of Slip Frequency PLL (b) Phase Mixer

2.2 Slip Frequency Phase Lock Loop (PLL)

The block Diagram of the Slip Frequency PLL, as shown in Fig.2-2 (a), is adapted from the traditional three-phase PLL of Fig. 2-1. Fig.2-2 (a) contains two phase Mixers (schematic shown in Fig.2-2 (b)), the operation of which is explained in 2.2.1. In Fig. 2-2 (a), the block labeled as VCO comprises the three blocks $[K_p+K_i/s]$, $[K_V]$ and [1/s] in Fig.2-1.

The 3-phase voltages on the stator side are transformed to the 2-phase α - β frame voltage vector $V_s[\cos(\omega_s t + \delta_s), \sin(\omega_s t + \delta_s)]^T$. After transformation from the a-b-c frame to the 2-phase α - β frame, the rotor currents are represented by the rotor current vector: $I_R[\cos(\omega_R t + \delta_R), \sin(\omega_R t + \delta_R)]^T$. The Phase Mixer adds the phase of the vector of the rotor currents $I_R[\cos(\omega_R t + \delta_R), \sin(\omega_R t + \delta_R)]^T$ to the phase of output vector of the VCO $[\cos(\omega_x t + \delta_x), \sin(\omega_x t + \delta_x)]^T$ to yield the vector $I_R\{\cos[(\omega_R t + \delta_R) + (\omega_x t + \delta_x)], \cos[(\omega_R t + \delta_R) + (\omega_x t + \delta_x)]\}^T$.

2.2.1 Phase Mixer

The "summers" and "multipliers" in Phase Mixer block of Fig.2-2 (b) implement phase addition (or subtraction) in 2-phase systems. This is based on the trigonometric identities:

As is well known, (2.2) also describes a rotational reference frame transformation. In fact, the Phase Mixer can be employed for transformations from the α - β frame to the γ - δ frame and vice-versa. This transformation will be used in the decoupled P-Q control (see Fig.4-4).

2.2.2 Phase Detector

The phase $[(\omega_R t + \delta_R) + (\omega_x t + \delta_x)]$ of the Phase Mixer output is compared with the phase of the output vector of the stator voltage $V_s[\cos(\omega_s t + \delta_s), \sin(\omega_s t + \delta_s)]^T$ in the Phase Detector. The Phase Detector outputs $\sin\{(\omega_s - \omega_x - \omega_R)t + (\delta_s - \delta_x - \delta_R)\}$ which is applied as an "error" to the input to the VCO control block in negative feedback. Inside the VCO control block (see detail in Fig. 2-1), the "phase error" passes through a Proportional-Integral (P-I) block. The output of the P-I block is added to a constant frequency ω_0 to become ω_x . The frequency ω_0 is set near to the stator frequency ω_s for fast frequency acquisition. After passing an Integrator Block, the output is $(\omega_x t + \delta_x)$ where the phase angle δ_x arises as a constant of integration. When the phase error is small, $\sin\{(\omega_s - \omega_x - \omega_R)t + (\delta_s - \delta_x - \delta_R)\}$ $\cong \{(\omega_s - \omega_x - \omega_R)t + (\delta_s - \delta_x - \delta_R)\}$. When the error is nulled by the negative feedback,

$$(\omega_{s}t + \delta_{s}) = (\omega_{r}t + \delta_{r}) + (\omega_{R}t + \delta_{R})$$
(2.3)

2.2.3 Speed Estimation

From (2.3), it follows that the Slip frequency PLL achieves the frequency equality $(\omega_s - \omega_x - \omega_R) = 0$ on tracking. As $\omega_s = \omega_R + \omega_m$ from induction machine theory, the solution of the two simultaneous equations is $\omega_x = \omega_m$, the rotor speed in electrical radians/s. There is PWM switching noise from the rotor currents in the signal ω_x which can be removed by a second-order filter as will be shown in Fig.3-11(Page 36). The filtering introduces a phase shift. If necessary the phase shift can be compensated for by a Lead-lag block as will be discussed in section 3.4.1.

The rotor frequency is $\omega_R = \omega_s - \omega_x$.

2.3 Proof of Concept of Slip Frequency PLL

Fig.2-3(a) shows the simulation of the rotor currents in the vector $[i_{R\alpha}, i_{R\beta}]^T = I_R[\cos(\omega_R t + \delta_R), \sin(\omega_R t + \delta_R)]^T$ when the DFIG is externally driven to undergo a transition

from sub-synchronous (positive slip) to super-synchronous (negative slip) rotor speed ω_m . Fig.2-3(b) shows the outputs $\cos(\omega_R t + \delta_R)$ and $\sin(\omega_R t + \delta_R)$ of the lower Phase Mixer of Fig.2-1(a). This Phase Mixer deducts the phase angle $(\omega_x t + \delta_x)$ of the VCO control block from the phase angle $(\omega_s t + \delta_s)$ of the stator PLL. In both Fig.2-3(a) and (b), the current $i_{R\alpha}$ lags $i_{R\beta}$ when the slip is positive and $i_{R\alpha}$ leads $i_{R\beta}$ when the slip has changed to negative. Comparing Fig.2-3(b) with Fig.2-3(a), one concludes that the Slip Frequency PLL tracks the frequency and phase of the rotor currents. Fig.2-3(c) also shows the rotor speed and the estimated speed ω_x . The estimate ω_x overlaps the rotor speed ω_m .

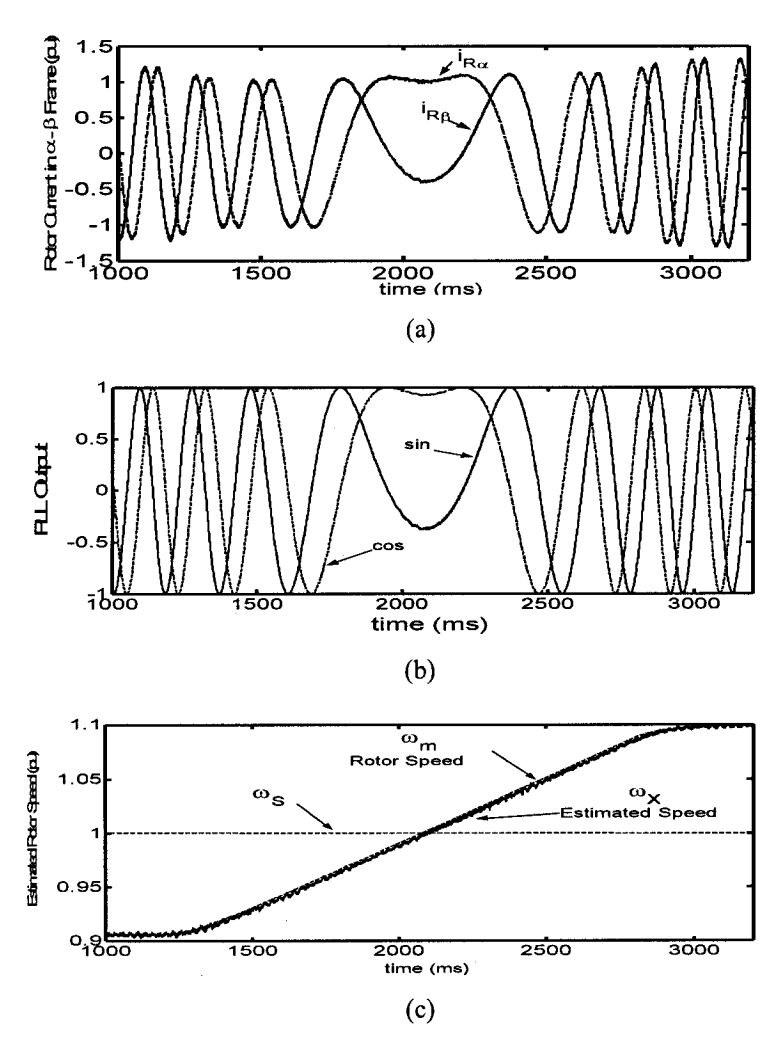


Fig.2-3 Proof of Slip Frequency PLL: (a) α - β frame rotor currents (b) Output of Rotor Slip PLL (c) Rotor Speed ω_m and estimated speed ω_x

2.4 α - β to γ - δ Transformation

2.4.1 Stator Voltage Transformation

For decoupled P-Q control, it is desirable to set up a synchronously rotating γ - δ frame by which the equations of the DFIG (see (2.4) below) has for its stator voltage vector the form $[V_{s\gamma}, V_{s\delta}]^T = V_s[1,0]^T$. In general, the 3-phase stator voltages on transformation to the α - β frame is $[V_{s\alpha}, V_{s\beta}]^T = V_s[\cos(\omega_s t + \delta_s), \sin(\omega_s t + \delta_s)]^T$. The Stator PLL in Fig.2-2 (a) acquires the information $[\cos(\omega_s t + \delta_s), \sin(\omega_s t + \delta_s)]$. As mentioned in relation to (2.2), the Phase Mixer operation is the same as a rotational frame transformation. Applying the Phase Mixer to transform the stator voltages from the α - β to the γ - δ frame:

$$\begin{pmatrix} V_{s\gamma} \\ V_{s\delta} \end{pmatrix} = \begin{pmatrix} \cos(\omega_s t + \delta_s) & \sin(\omega_s t + \delta_s) \\ -\sin(\omega_s t + \delta_s) & \cos(\omega_s t + \delta_s) \end{pmatrix} \begin{pmatrix} V_{s\alpha} \\ V_{s\beta} \end{pmatrix} = \begin{pmatrix} V_s \\ 0 \end{pmatrix}$$
 (2.4)

The synchronously rotating $\gamma - \delta$ frame is established.

2.4.2 Rotor Current Transformation

The rotor current vector, which originally is $I_R[\cos(\omega_R t + \delta_R), \sin(\omega_R t + \delta_R)]^T$, has been transformed by the upper Phase Mixer in Fig. 2-2 (a) to $I_R[\cos\{(\omega_x t + \delta_x) + (\omega_R t + \delta_R)\}, \sin\{(\omega_x t + \delta_x) + (\omega_R t + \delta_R)\}]^T$. The γ - δ frame rotor currents is obtained by using a Phase Mixer to subtract the phase $(\omega_s t + \delta_s)$ acquired by the Stator PLL. The resultant vector is $I_R[\cos\{(\omega_x t + \delta_x) + (\omega_R t + \delta_R) - (\omega_s t + \delta_s)\}]$, $\cos\{(\omega_x t + \delta_x) + (\omega_R t + \delta_R) - (\omega_s t + \delta_s)\}]^T$. Since $\omega_x + \omega_R - \omega_s = 0$, it follows that the transformed current vector is $[i_{R\gamma^*}, i_{R\delta^*}]^T = I_R[\cos(\delta_x + \delta_R - \delta_s), \sin(\delta_x + \delta_R - \delta_s)]^T$, which are in the synchronously rotating γ^* - δ^* frame of the rotor currents. The asterisks * in γ^* and δ^* are to emphasize that although the rotor currents are in the synchronously rotating frame, the frame is not aligned to the desired stator voltage γ - δ axes of (2.4). Fig.

2-4 illustrates the γ^* - δ^* frame which is separated from the γ - δ frame (defined by (2.4)) by an angle Φ . The currents in the frame *with* asterisks and in the frame *without* asterisks are related by the angle rotation matrix in (2.5), an operation which can be implemented by the Phase Mixer of Fig. 2-2 (b):

$$\begin{pmatrix} i_{R\gamma} \\ i_{R\delta} \end{pmatrix} = \begin{pmatrix} \cos \Phi & \sin \Phi \\ -\sin \Phi & \cos \Phi \end{pmatrix} \begin{pmatrix} i_{R\gamma^*} \\ i_{R\delta^*} \end{pmatrix}$$
 (2.5)

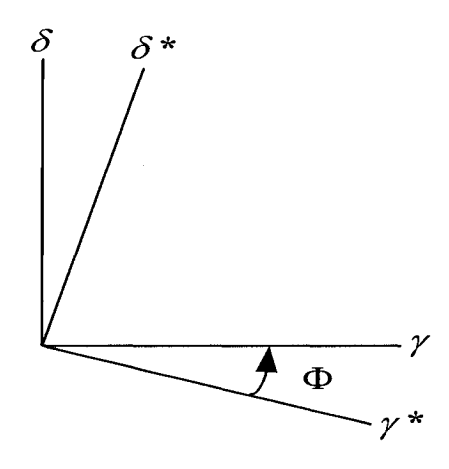


Fig.2-4 γ - δ and γ *- δ *axes frames separated by ϕ

2.4.3 γ - δ Axes Aligner

This thesis is oriented towards applying decoupled P-Q control to the DFIG. It is to be recalled that in the $\gamma-\delta$ reference frame, the stator-side real and reactive power are respectively $P_s=v_{s\gamma}i_{s\gamma}+v_{s\delta}i_{s\delta}$ and reactive $Q_s=v_{s\gamma}i_{s\delta}-v_{s\delta}i_{s\gamma}$. Decoupled P-Q control consists of making $v_{s\delta}=0$ so $P_s=v_{s\gamma}i_{s\delta}$ and $Q_s=v_{s\gamma}i_{s\delta}$. Therefore when the $\gamma-\delta$ axes are aligned such that $v_{s\delta}=0$, the stator-side real and reactive power are obtained by controlling the currents $i_{s\gamma}$ and $i_{s\delta}$. Decoupled P-Q control requires establishing the $\gamma-\delta$ axes for which $v_{s\delta}=0$, which is simple enough to do with an absolute position encoder to locate the axis of the a-phase rotor winding. The challenge in sensorless drive

research is to use electrical measurements to estimate mechanical measurements of position and velocity.

The mathematical model of the DFIG in the γ - δ frame will be presented as (4.12) in the chapter 4. The method of aligning the γ - δ axes is well known [10] and consists setting $v_{s\delta} = 0$ in the second row in (4.12). However, it has been found that it is more reliable to use the equivalent by using first row of (4.12). This consists of equating $v_{s\gamma}$ as computed in the first row of (4.12) to its measured value V_s .

The voltage v_{sy} evaluated using the first row of (4.12) is:

$$v_{s\gamma} = R_s i_{s\gamma} - \omega_s (L_m i_{R\delta}^* + L_s i_{s\delta})$$
 (2.6)

It is based on omitting the d/dt termsin (4.12).

The voltage V_s is calculated from (2.4), where $(v_{s\alpha}, v_{s\beta})$ have been transformed from the a-b-c frame stator voltage measurements and $(cos(\omega_s t + \delta_s), sin(\omega_s t + \delta_s))$ are taken from the stator voltage PLL.

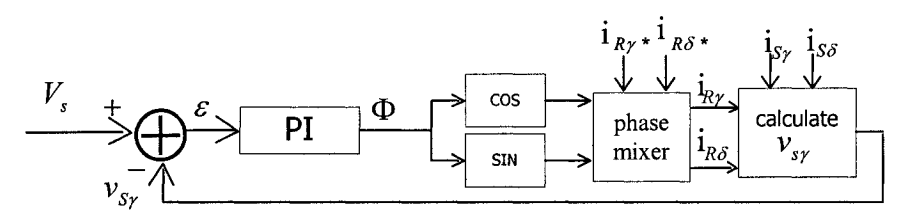


Fig.2-5 Block diagram of γ-δ Axes Aligner

As shown in Fig. 2-5, the computed value of v_{sy} is compared with V_s and the error ε after passing through a P-I Block becomes the angle Φ . The phase mixer rotates the phase angle of i_{Ry}^* , $i_{R\delta}^*$ by the angle Φ to yield an estimate of i_{Ry} , $i_{R\delta}$ in the v_{sy} computation block which evaluates (2-6). When $v_{sy} = V_s$, the equivalent $v_{s\delta} = 0$ is satisfied and the γ - δ axes is located for decoupled P-Q control to be implemented.

After aligning the rotor to the stator γ - δ axes, it can be shown by back substitution that:

- (1) $\Phi + (\omega_x t + \delta_x)$ is the position of the rotor a-axis with respect to the stator a-axis.
- (2) the α - β rotor frame voltage vector is:

$$[v_{R\alpha}, v_{R\beta}]^T = [v_{R\gamma}\cos\{(\omega_s t + \delta_s) - \Phi - (\omega_x t + \delta_x)\}, v_{R\delta}\sin\{(\omega_s t + \delta_s) - \Phi - (\omega_x t + \delta_x)\}]^T$$
(2.7)

2.4.4 Proof of Concept-- γ - δ Axes Aligner

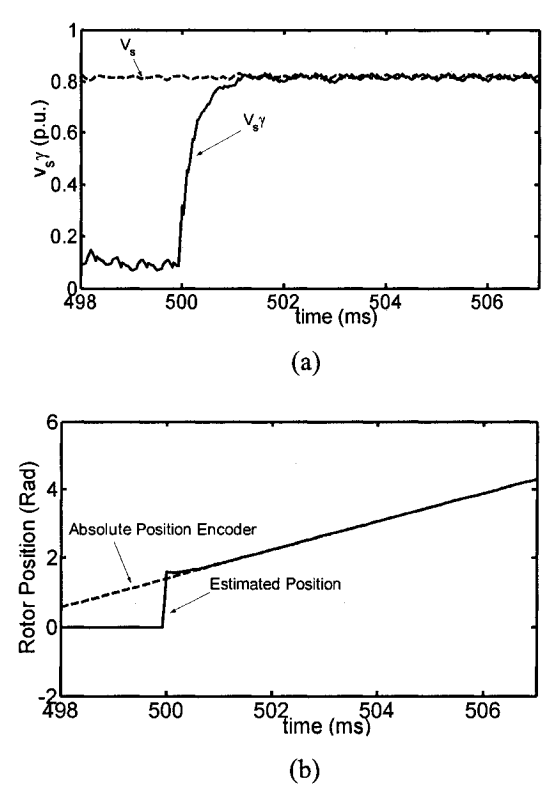


Fig.2-6 Proof of γ - δ Axes Aligner (a) $v_{s\gamma}$ and v_s (b) Rotor Position (absolute Position encoder, estimated)

In a simple test, the rotor of the DFIG is given a constant speed. Fig. 2-6 (a) shows the voltage $v_{s\gamma}$ before and after the activation of the γ - δ axes aligner. In the same experiment, Fig. 2-6 (b) shows the estimated position of the DFIG rotor a-axis based on the formula Φ + $(\omega_X t + \delta_X)$. The software module of the DFIG is equipped with an absolute position encoder and its position is also displayed. The fast convergence of $v_{s\gamma}$ to V_s and the overlap of the two graphs of rotor positions are indirect proofs of the success of the γ - δ axes aligner.

2.4.5 Influence of error in R_s , L_{ls} and L_m on Estimated Rotor Position

From the previous section, the location of the γ - δ axes is based on the equality $v_{s\gamma}=R_si_{s\gamma}-\omega_s(L_mi_{R\delta}^*+L_si_{s\delta})$. This implies that R_s , L_s and L_m must be

measured accurately before the decoupled P-Q control of the DFIG can be implemented. Furthermore, saturation and nonlinearity of iron core, as well as temperature-dependence of resistors, may cause deviations from the measured inductances and resistances in the DFIG. It is most desirable that the method is robust, i.e. the implementation is not too sensitive to parameter variation. In the following subsections, three different experiments have been performed to evaluate the sensitivity to the parameters R_s , L_s and L_m . The index chosen for evaluation is the rotor position which is estimated from the equation $\Phi + (\omega_x t + \delta_x)$ where Φ is obtained from the γ - δ Axes Aligner of Fig.2-5 and $(\omega_x t + \delta_x)$ is obtained from the Slip Frequency PLL of Fig. 2-2 (a).

2.4.5.1 Case Study-- Parameter Sensitivity -- R_s

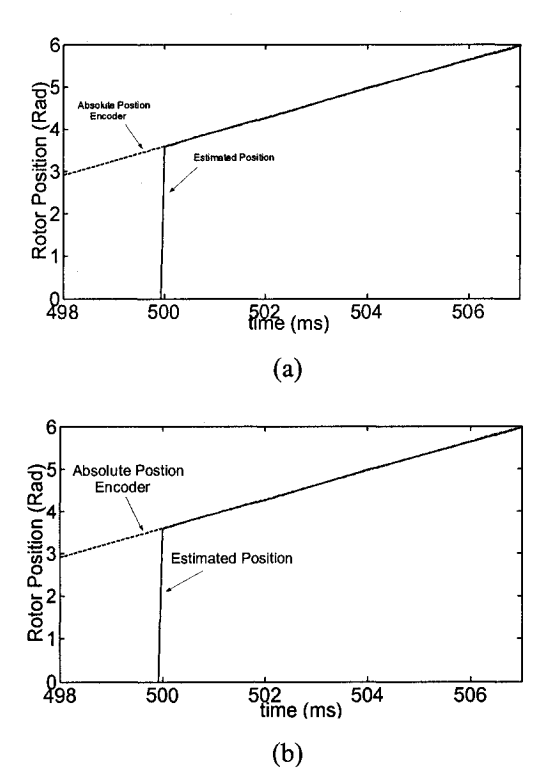


Fig.2-7 Simulated waveforms of estimated (solid lines) and actual (dotted lines) rotor position (a) $R_S = 0$; (b) $R_S = 2$ X actual value.

As we know, resistances are sensitive to temperature variation. It means that the value of R_s is not fixed, but may be change with time. Fortunately, for the induction machine, R_s and R_R are designed to be small to decrease power loss. In the case study, R_s and R_R

are 0.0085, 0.01 p.u., respectively. Fig.2-7(a) and (b) shows the effect of variation in R_s on the estimation process. In the first case, R_s used in the estimation algorithm is 0 and, in the second case, it is 2 times of the actual value. The plots show almost negligible errors in the computation of the rotor position, even at starting.

2.4.5.2 Case Study Parameters Sensitivity – L_{IS} and L_{m}

 L_{IS} is the per phase stator winding leakage inductance. L_{IS} is less sensitive to temperature variation than R_S . Iron saturation affects both the leakage inductance L_{IS} and the magnetizing inductance L_m , the latter more so than the former.

Estimated and measured values of the rotor position are compared in two tests for the variation of the parameter L_{lS} . In the first case L_{lS} in the control circuit is changed from nominal value of 0.086 p.u. to 0.0 p.u. In the second case, L_{lS} takes the value 0.172 p.u. (2 times 0.086 p.u.). Fig. 2-8 (a) and (b) show the difference between estimated and real rotor position based on the influence of the error on the leakage inductance of L_{lS} .

Another two tests have been performed to assess the sensitivity of the magnetizing inductance L_m . The differences between the estimated and real rotor position are represented in Fig.2-9(a) and (b), respectively for the value L_m =4.75 p.u. (1.5 times actual value) and the value L_m =1.55 p.u. (0.5 times actual value). The plots in Fig.2-8 and Fig.2-9 show that the influence of the error on L_{lS} and L_m is almost negligible in the estimation of the rotor position, even at starting.

2.5 Explanation for Robustness

It is well known that R_s , $\omega_s L_{ls}$ are very much smaller than $\omega_s L_m$. The parameters in Appendix A bear this out. Because $\omega_s L_m$ dominates in size, it follows that the magnetizing current $i_{m\delta} = (i_{R\delta} + i_{s\delta})$ is small. In general, $i_{R\delta}$ is comparatively large

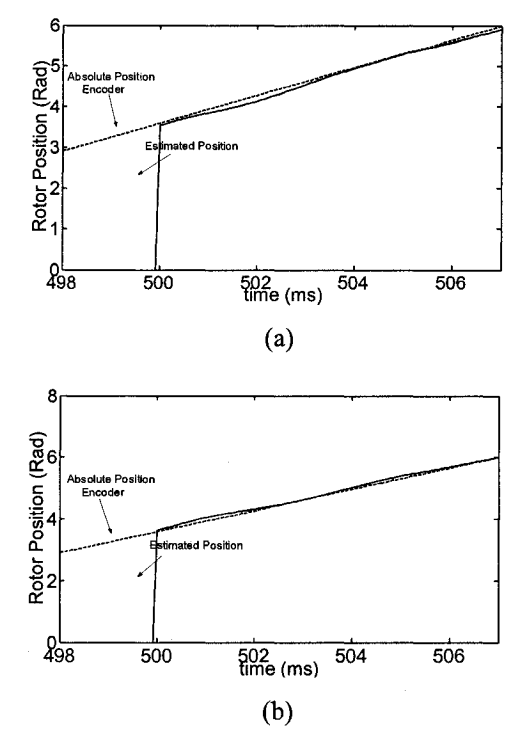


Fig.2-8 Simulated waveforms of estimated (solid lines) and actual (dotted lines) rotor position (a) L_{ls} = 0 and (b) L_S =2 X actual value

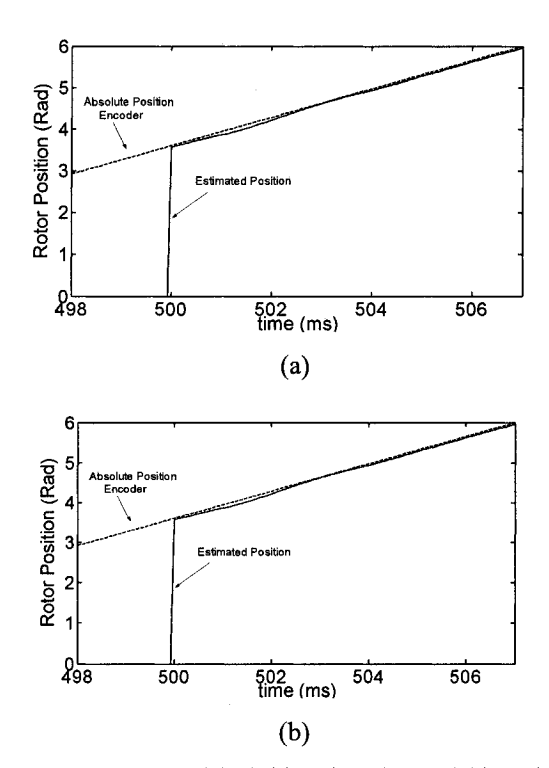


Fig.2-9 Simulated waveforms of estimated (solid lines) and actual (dotted lines) rotor position (a) L_m =0.5 X actual value (b) L_m =1.5 X actual value

and roughly equal and opposite to $i_{s\delta}$. The robustness shown in Fig. 2-7, 2-8 and 2-9 follows from the relative parameter sizes which are typical in induction machines.

When R_s is small, $v_{s\gamma}=R_s i_{s\gamma}-\omega_s(L_m i_{R\delta}^*+L_s i_{s\delta})$ of (2.6) is approximately the same as $v_{s\gamma}\approx-\omega_s(L_m i_{R\delta}^*+L_s i_{s\delta})$. This is the explanation for the robustness shown in Fig. 2-7.

Because $\omega_s L_{ls}$ is small compared to $\omega_s L_m$, it follows that $\omega_s L_s = \omega_s L_{ls} + \omega_s L_m$ can be approximated as $\omega_s L_s \approx \omega_s L_m$. Thus $v_{s\gamma} = R_s i_{s\gamma} - \omega_s (L_m i_{R\delta}^* + L_s i_{s\delta})$ is approximately the same as $v_{s\gamma} \approx R_s i_{s\gamma} - \omega_s L_m (i_{R\delta}^* + i_{s\delta})$. This explains the robustness shown in Fig.2-8.

Because R_s and $\omega_s L_{ls}$ are small, dividing $v_{s\gamma} \approx R_s i_{s\gamma} - \omega_s L_m (i_{R\delta}^* + i_{s\delta})$ by the large magnetizing reactance $\omega_s L_m$, one has the approximate magnetizing current $i_{m\delta} = v_{s\gamma} / \omega_s L_m$ on the left-hand-side. Equating it to the right-hand-side, the equation becomes $i_{m\delta} \approx (i_{R\delta}^* + i_{s\delta})$. Inaccuracy in the large magnetizing reactance $\omega_s L_m$ has minor influence only since $i_{m\delta}$ is the small difference between the large, almost equal and opposite $i_{R\delta}^*$ and $i_{s\delta}$ in the relation $i_{m\delta} - i_{R\delta}^* \approx i_{s\delta}$. This explains the robustness shown in Fig. 2-9.

2.6 Conclusion

This chapter has described an innovative Slip Frequency Phase Lock Loop (PLL) which measures the slip frequency correctly even as the rotor speed passes from subsynchronous to super-synchronous speed. It also has excellent phase tracking capability. Furthermore, the Slip Frequency PLL has fast response and very good immunity against high frequency noise, the same as the conventional PLL. Simulations, in test circuits where the rotor currents are controlled by a Voltage-Source Converter, have shown that it works well even when the rotor currents contain large PWM switching noise. The θ -output of the PLL has no phase error and negligible high frequency ripples. Its

performance proves that it can be used in power electronics systems with large PWM noise.

This chapter has also proposed a $\gamma - \delta$ Axes Aligner, which used in conjunction with the Slip Frequency Phase Lock Loop (PLL), makes sensorless P-Q control of the DFIG possible. The DFIG can be operated even at synchronous speed, which corresponds to operating at zero rotor frequency. In most situations, the DFIG rides through synchronous speed from sub-synchronous speed to super-synchronous speed and vice-versa.

This chapter has shown that the estimation of rotor position is not sensitive to machine parameters.

Speed Estimation by Slip Frequency Phase Lock Loop (PLL)

3.0 Introduction

In most motor drive systems, automatic control requires speed and/or position sensors in the feedback loops. Eliminating speed and/or position sensor results in lower cost and increased reliability and ruggedness in the overall drive system.

As discussed in Chapter 2, the rotor speed can be estimated by a Slip Frequency Phase Locked Loop (PLL). This method compares favourably with methods [6,8,9] which estimate the rotor position first and then obtain the rotor speed by differentiation.

The first objective of this chapter is to evaluate the accuracy of speed measurement by the Slip Frequency Phase Locked Loop (PLL). The first step is to design a simulation experiment by which errors in speed estimation can be measured. The simulation software EMTP(R) has a model of a wound rotor induction machine which can represent a doubly-fed induction generator (DFIG). The rotor speed can be precisely controlled by a dc machine (software) coupled to the shaft of a DFIG (software). The rotor speed is measured by a speed sensor (software) which is used as the benchmark against which the error of the estimated speed of the Slip Frequency Phase Locked Loop (PLL) is measured. The software "equipment" have been assembled to measure the accuracy of speed estimation by the Slip Frequency PLL.

As the Slip Frequency Phase Locked Loop (PLL) is intended to be a component of the sensorless decoupled P-Q control of a DFIG, the test is orientated to finding how accurately the Slip Frequency PLL estimates the speed in the dynamic situation. For this reason, the error (against the measurement from the software speed sensor) is presented as a function in the frequency domain, as in a Bode Diagram. This is obtained by using the software dc machine to produce an oscillating perturbation speed over a frequency range. It is found that there is a significant inaccuracy when the oscillation speed frequency is high. The error appears in the form of a phase lag which increases with frequency. This suggests that there is a time delay in the sensorless method of speed measurement. The

recent publication by the author [12], it has stated that the time delay did not prevent the implementing of a decoupled P-Q controlled DFIG for wind-turbine applications.

However, from a fundamental research standpoint, it is important to pinpoint the sources of the inaccuracy and this forms the second objective of this chapter. There are 2 places where the time delay may be introduced: (i) the P-I Block in the VCO of the Slip Frequency PLL; (ii) the time constants related to leakage inductances of the DFIG. By analysis using the mathematical model of the Slip Frequency Phase Lock Loop and by simulations, it has been established that the culprit is in the leakage inductances of the DFIG. Since the leakage inductances of the electric machine cause the machine currents to lag the applied voltage and since "sensorless" speed and position measurements rely on measurements of currents and voltages, one concludes that this type of error is inherent in "sensorless" methods, even in those of [6,8,9].

In addition to this delay, there is a *second* delay which is common to sensorless methods when used in conjunction with power electronic controllers. This is the time delay from the filter required to remove the noise associated with the PWM switching before the voltage and/or current measurements can be used by the sensorless methods.

The advantage of the Slip Frequency PLL is that it does not have a *third* delay as in the speed measurements of [6,8,9], which have been obtained by differentiating the estimated of rotor position. Differentiation is an inherently noisy operation and requires filtering which introduces the *third* time delay.

The final part of this chapter addresses the composite *first* and *second* time delays. Simulation shows that a lead-lag block can compensate for the composite time delay.

3.1 Calibrating Slip Frequency PLL

An experimental set up by simulation, as shown in Fig.3-1, has been designed to evaluate the accuracy of the speed estimated by the Slip Frequency PLL. The DFIG is represented by the software model of a slip ring wound rotor induction machine (SRIM). The speed measured by a software speed sensor, coupled to the shaft, is used as the speed standard for comparison. On the stator side, the SRIM is excited by a balanced 3-phase ac

source. The slip rings of the induction machine (SRIM) are connected to a bank of balanced 3-phase resistors. Thus the Slip Frequency PLL has the stator voltage, stator current and rotor current measurements required for speed estimation.

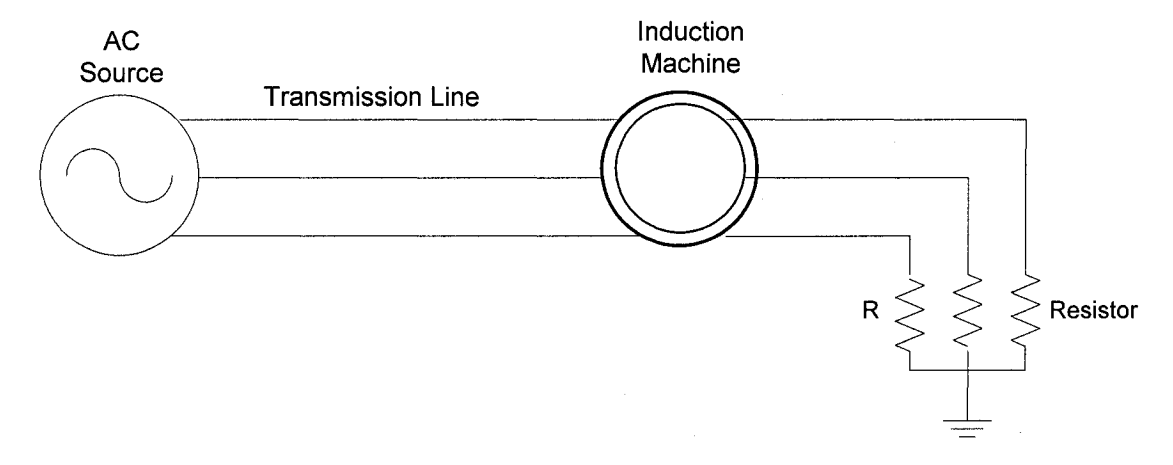


Fig.3-1 Configuration of Induction Machine system

The induction machine (SRIM) is driven by a software external DC motor. To study the response of estimating rotor speed under different conditions, the DC motor, which supplies the mechanical torque T_m to the induction motor, is operated under speed feedback control. Fig.3-2 shows the torque control block diagram.

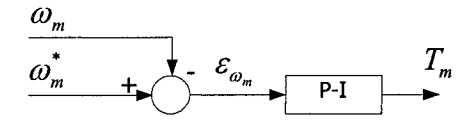


Fig.3-2 Torque Control Block Diagram

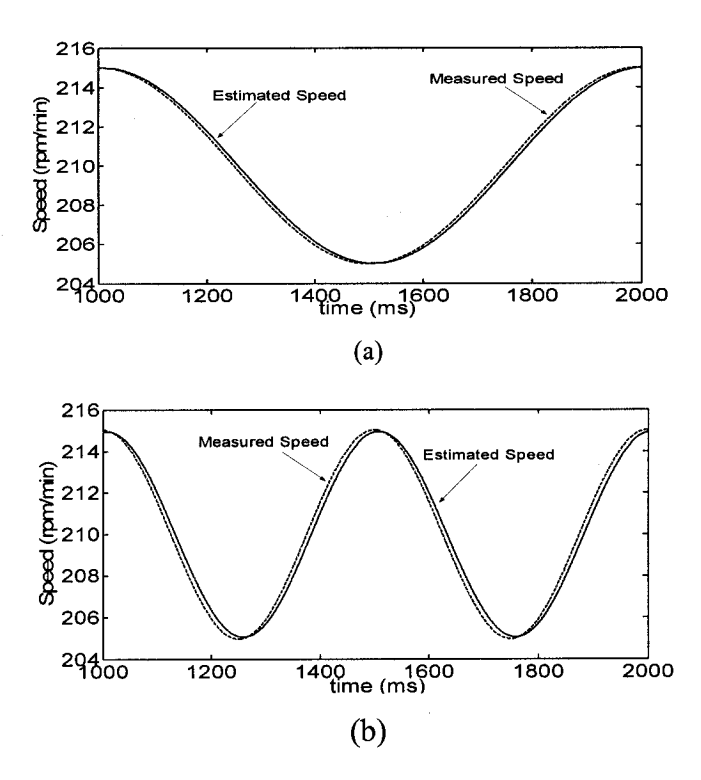
This block accepts the measured rotor speed ω_m (from the software speed sensor) and the reference rotor speed ω_m^* as inputs and outputs the mechanical torque T_m . The error $\varepsilon_{\omega_m} = \omega_m^* - \omega_m$, after passing through P-I (proportional-integral) block, is taken as the input torque of the induction machine. By applying this block, the actual speed will follows the reference speed ω_m^* accurately. The constants K_p and K_i in the P-I block (Fig.3-2) have been obtained by trial and error.

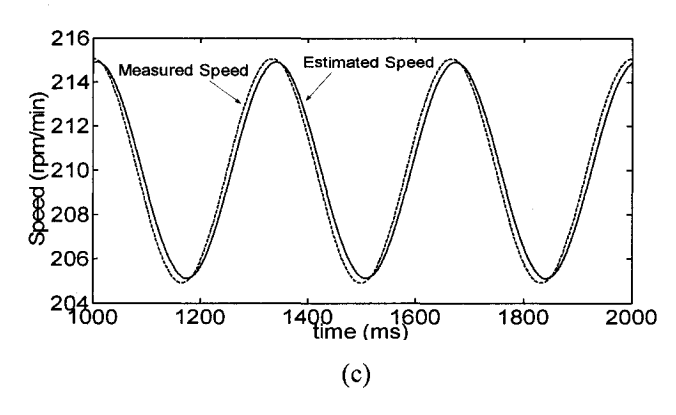
3.2 Frequency Domain Evaluation of Slip Frequency PLL

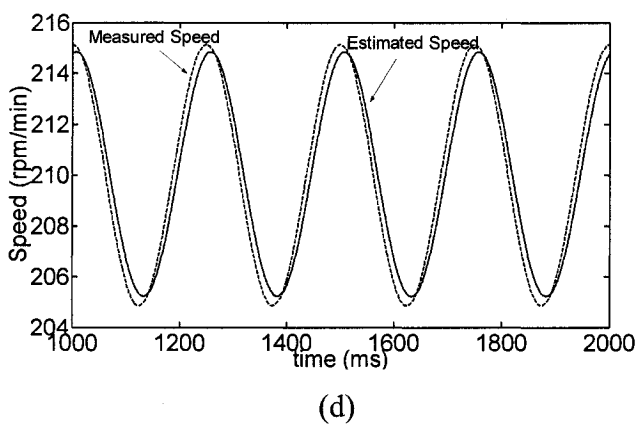
The simulation experiments planned for the Slip Frequency PLL consist of using the dc motor to drive the induction machine (SRIM) at an average speed of 210 rad/sec. (The SRIM operates as an induction generator as this average speed is above the synchronous speed of 188.8 rad/sec.) In addition, the speed is varied sinusoidally between 205 and 215 rad/sec. With this fixed amplitude of 5 rad/sec, the frequency of the sinusoidal variation is changed.

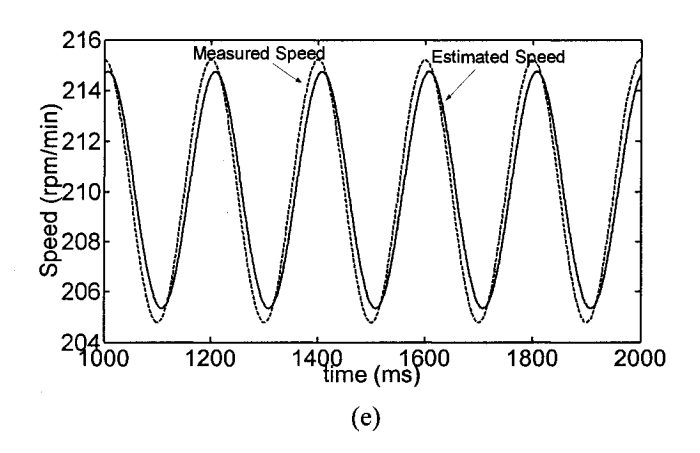
Fig.3-3 (a),(b),(c),(d),(e),(f),(g) and (h) are records of the estimated speed and actual speed under f=1hz, 2hz,3hz,4hz,5hz,10hz and 15hz, respectively.

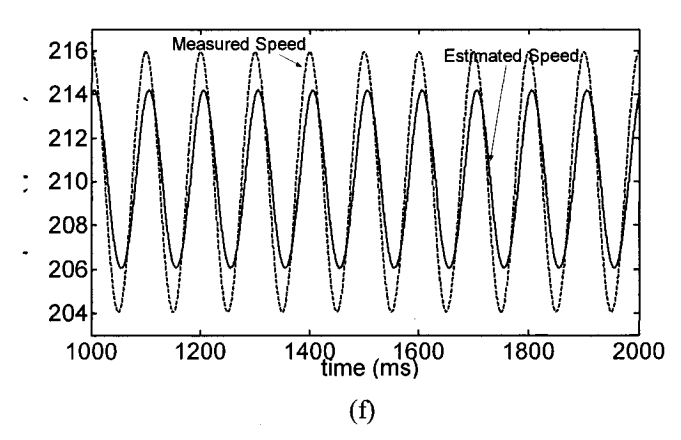
From the data of Fig.3-3, one constructs the Bode Diagram. As the perturbation magnitudes of speed do not differ much, the Bode Diagram of the Magnitude Error is omitted. Fig.3-4 shows the Error in the Phase Angle which increases with frequency. The monotonic increase in the phase error with frequency, although not linear, suggests that the phase error is due to a time delay. This time delay can be from the P-I Block in the VCO of the Slip Frequency PLL in Fig.2-2(a). The second possible source is the leakage inductance of the induction machine. In the next section, the analytical model for Slip Frequency PLL is developed and examined to find out if the delay has its origin in the Slip Frequency PLL.











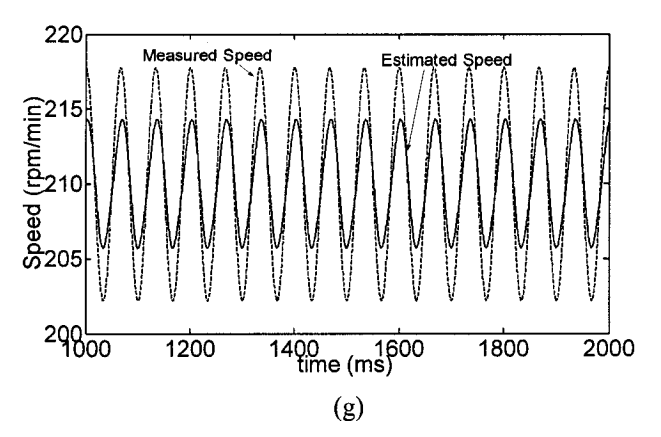


Fig.3-3 Estimated Speed and Actual Speed under different Frequencies: (a) f=1Hz, (b) f=2Hz, (c) f=3Hz, (d) f=4Hz, (e) f=5Hz, (f) f=10hz, (g) f=15Hz.

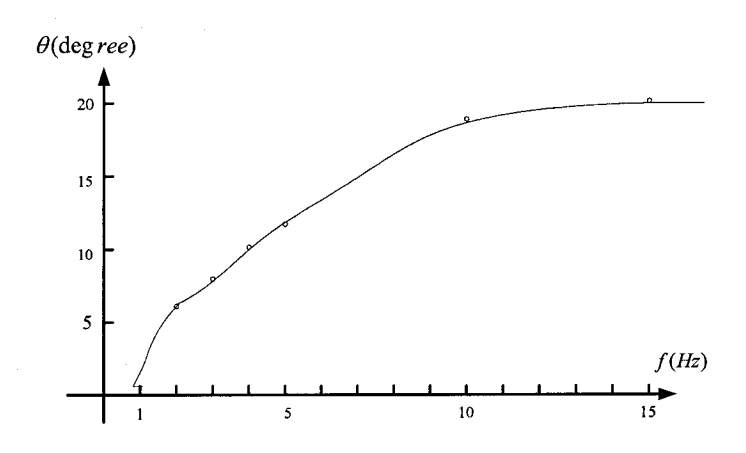


Fig.3-4 Phase Difference between Estimated Speed and Actual Speed (Bode-diagram)

3.3 Analytical Model of Slip Frequency PLL

The master thesis of Jian Hu [11] has a linearized model of the conventional PLL. As the Slip Frequency PLL is an adaptation of the conventional PLL, the same methodology can be applied to the Slip Frequency PLL.

3.3.1 Linearized Model of Slip Frequency Phase Lock Loop

It is well known that the information carried by the input signal of the Phase Lock Loop is neither the magnitude, nor the frequency, but the phase. At this point, it is useful to remember that "phase angle" and is the time integral of the "angular frequency".

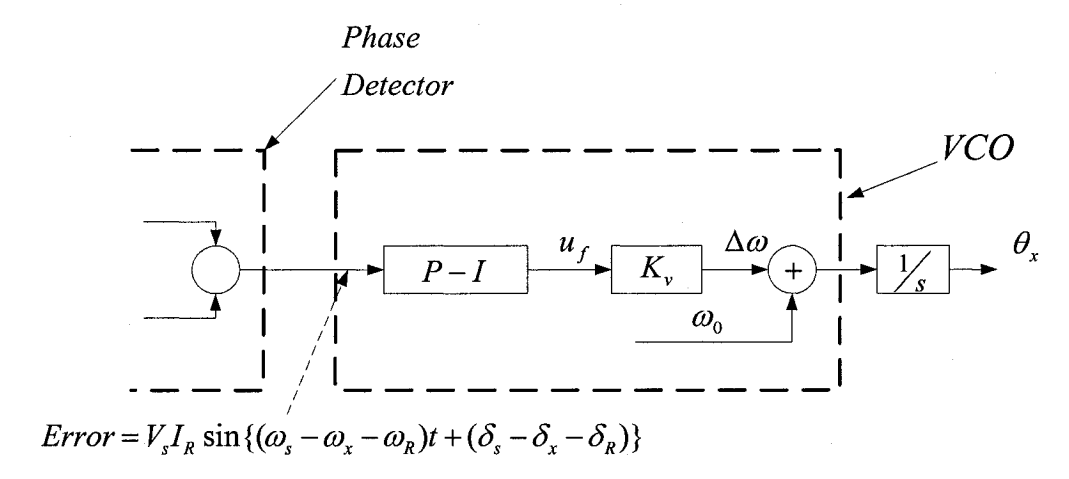


Fig. 3-5 Block Diagram of VCO

The analysis centers around the VCO of Fig.2-2 which is redrawn in detail as in Fig.3-5. The central frequency term, ω_0 , which is added to $\Delta\omega$ in Fig. 3-5, complicates the linear analysis. The complication is lessened by defining the phase angles (θ_1 and θ_2) and the angular frequency (ω_1 and ω_2) shown in the linearized model in Fig. 3-6 using the operations as follows:

$$\theta_1(t) = (\omega_s(t) - \omega_p(t))t + (\delta_s - \delta_p) - \omega_0 t. \tag{3.1}$$

$$\theta_2(t) = \theta_X(t) - \omega_0 t \tag{3.2}$$

$$\omega_1(t) = \frac{d\theta_1(t)}{dt} = \omega_s(t) - \omega_R(t) - \omega_0$$
(3.3)

$$\omega_2(t) = \frac{d\theta_2(t)}{dt} = \omega_x(t) - \omega_0 \tag{3.4}$$

The central frequency ω_0 is assumed to be constant. Applying (3.1) to (3.4) to remove the central frequency, the angular velocity of the input and the output of the Slip Frequency PLL are characterized by the variables ω_1 and ω_2 respectively. The next step is to derive the transfer function that relate ω_1 and ω_2

3.3.1.1 Transfer Function of Phase Detector:

The output of Phase Detector is $V_sI_R\sin\{(\omega_s-\omega_x-\omega_R)t+(\delta_s-\delta_x-\delta_R)\}$ where V_s is the magnitude of the stator-side voltage and I_R is the magnitude of the rotor-side current. The sine function of the Phase Detector is a nonlinear element. However upon frequency acquisition, once the phase error is small, $\sin\{(\omega_s-\omega_x-\omega_R)t+(\delta_s-\delta_x-\delta_R)\}\cong\{(\omega_s-\omega_x-\omega_R)t+(\delta_s-\delta_x-\delta_R)\}$. Then the Phase Detector block can be linearized as follows:

$$error = V_s I_R (\omega_s t - \omega_R t - \omega_x t + \delta_s - \delta_R - \delta_x)$$
(3.5)

Substituting (3-1) and (3-2), the equation can be rewritten as

$$error = V_s I_p(\theta_1 - \theta_2)$$
 (3.6)

3.3.1.2 Close Loop Transfer Function of Linearized Slip Frequency PLL

By removing the constant central frequency ω_0 and by linearizing the phase detector, the close loop transfer function blocks of the linearized Slip Frequency PLL is shown in Fig.3-6:

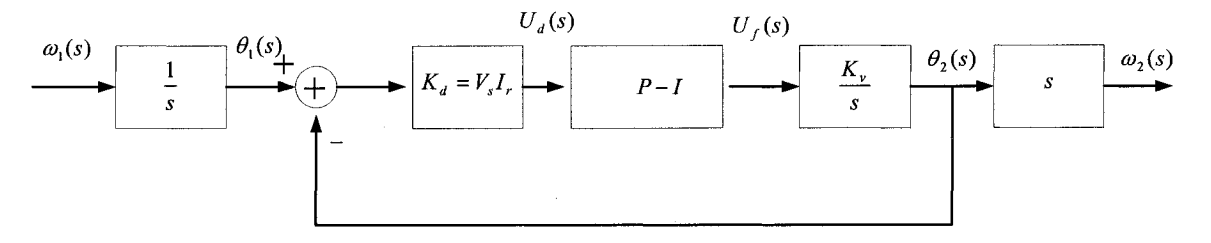


Fig.3-6 Linearized Model of SLIP Frequency Phase Lock Loop

3.3.1.3 Transfer Function of P-I Block:

The transfer function of the P-I block yields:

$$\frac{U_f(s)}{U_d(s)} = K_p + \frac{K_I}{s} \tag{3.7}$$

where K_p is proportional gain

 K_I is integration gain.

3.3.1.4 Transfer Function of Linearized Slip Frequency PLL

The input of the combination of the sum, the Pure Gain block and the Integral block is the output of P-I block. From Fig.3-5, the output of the whole combination is actually output of the PLL which can be expressed as:

$$\theta_{x}(t) = \int_{-\infty}^{t} [\omega_{0} + \Delta\omega(\gamma)] d\gamma = \omega_{0}t + \int_{-\infty}^{t} K_{v} u_{f}(\gamma) d\gamma$$
 (3.8)

Assuming the central frequency of VCO, $\omega_{\scriptscriptstyle 0}$, to be constant, then

$$\theta_{2}(t) = \theta_{y}(t) - \omega_{0}t \tag{3.9}$$

By substituting eq.(3.9) into the above equation (3.8), the feedback can be rewritten:

$$\theta_2(t) = \int_{-\infty}^{t} K_{\nu} u_f(\gamma) d\gamma \tag{3.10}$$

Then the transfer function of the combination can be demonstrated as:

$$\frac{\theta_2(s)}{U_s(s)} = \frac{K_v}{s} \tag{3.11}$$

The closed loop the transfer function of Fig. 13 is:

$$\frac{\omega_2(s)}{\omega_1(s)} = \frac{\theta_2(s)}{\theta_1(s)} = \frac{K_d K_v (K_I + K_p s)}{s^2 + s K_d K_v K_p + K_d K_v K_I}$$
(3.12)

$$=\frac{2\xi\omega_n s + \omega_n^2}{s^2 + 2\xi\omega_n s + \omega_n^2} \tag{3.13}$$

where: the natural frequency $\omega_n = \sqrt{\frac{K_d K_v}{\tau}}$

the damping ratio
$$\xi = \frac{1}{2\tau\omega_n}$$

3.3.1.5 Parameters Design

From eq.(3.12), the transfer function is a second-order system. The Slip Frequency PLL is designed to lock to a signal with the frequency range from 42Hz to 78Hz(due to the limited range of the machine slip s). The central frequency is chosen to be 60Hz, and the damping factor to be 0.707. Following the design procedure of Jian Hu [11], the parameters of P-I block $K_I = 30.78$ and $K_p = 0.1633$ are chosen, and then the close loop transfer function of the linearized Slip Frequency PLL can be expressed as:

$$\frac{\omega_2(s)}{\omega_1(s)} = \frac{377s + 71054}{s^2 + 377s + 71054} \tag{3.14}$$

The Bode-Diagram of the eq.(3.14) is shown in Fig.3-7.

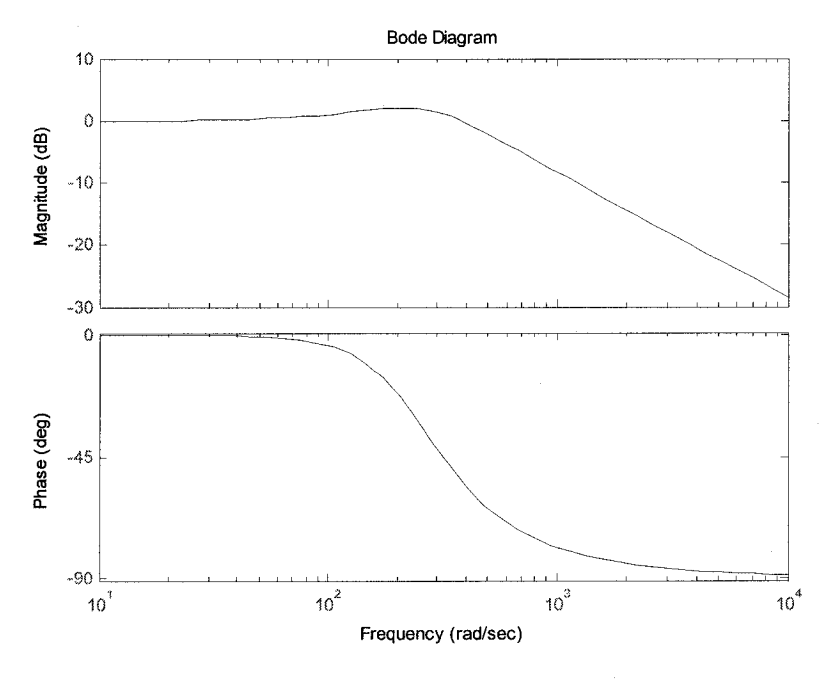


Fig.3-7 Bode diagram of transfer function of linearized Slip Frequency PLL

From the phase angle of the Bode diagram in Fig.3-7, one sees that up to 15 Hz the phase shift is very small. It should be recalled that the frequency deviations are from the central frequency of 60 Hz. The rotor speed ω_m is related to ω_2 of Fig. 3-6 by (3.4) through the equation $\omega_m = \omega_X = \omega_2 + \omega_0$. Therefore, one concludes that the phase shifts in the speed measurements in Fig.3-4 are not from the Slip Frequency PLL.

3.3.2 Phase Shift Caused by Time Delay in Current Measurement

The "sensorless" measurements of rotor speed and position are computed from motor currents and voltages. Instantaneous rotor speed ω_m appears electrically as instantaneous Blv voltages (where the velocity $v=\omega_m r$ and r is the radial distance of the conductors) induced across the rotor conductors. The rotor circuit has a time constant $T_R = L_{IR}/R_R$ associated with the rotor leakage inductance L_{IR} and resistance R_R . Likewise, the stator circuit has a time constant $T_S = L_{IS}/R_S$ associated with the stator leakage inductance L_{IS} and resistance R_S . Because the DFIG currents lag the instantaneous rotor speed ω_m , the estimated speed from the "sensorless" measurement method will have phase lags associated with the time constant delays. To prove the hypothesis, the simulations of Fig.3-1 have been repeated in a second induction machine, DFIG2. DFIG2 is identical to the original machine of Fig.3-1, which is labeled as DFIG1, except that the leakage inductances are reduced by a factor of 0.01. The parameters of the two DFIGs are listed in per unit values in Table.1.

	DFIG 1	DFIG 2
Stator leakage inductance L_{IS} (p.u.)	0.085	0.00085
Rotor leakage inductance L_{lR} (p.u.)	0.11	0.0011
Stator resistance R_s (p.u.)	0.01	0.01
Rotor resistance R_R (p.u.)	0.00662	0.00662
Magnetizing inductance L_m (p.u.)	3.1	3.1

Table 1 Parameters of two Induction Machines

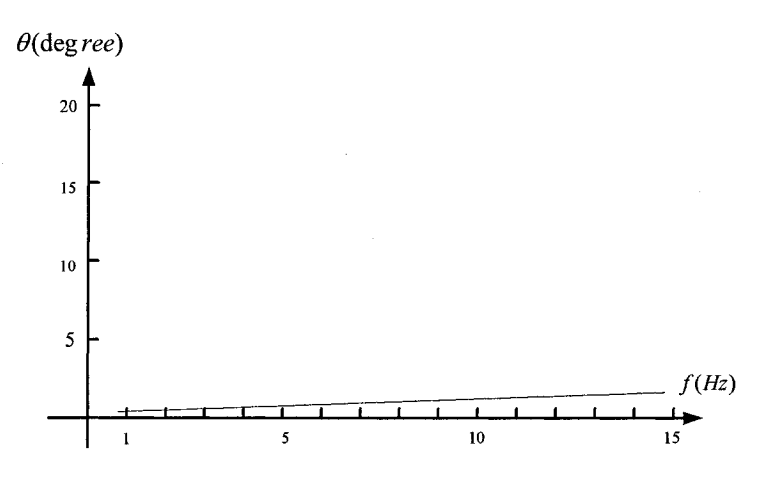


Fig.3-8 Phase Difference Shift between Estimated Speed and Actual Speed versus Frequency for DFIG 2

Fig.3-8 shows the phase angle error in the form of a Bode-diagram. Comparing it with Fig.3-4, it is clear that the reduced leakage inductance reduces the phase shift significantly. This simulation proves the hypothesis that the time delay in the current measurements is the source of the phase shift error.

3.4 Speed Estimation of DFIG Connected to Voltage-Source Converter (VSC)

Up to this point, speed measurement by the Slip Frequency PLL is for the induction machine connected as shown in Fig.3-1. In decoupled P-Q control of a DFIG, the rotor slip rings are connected to a Voltage-Source Converter (VSC) as shown in Fig.1-1. The rotor currents will contain the switching noise of Pulse Width Modulation (PWM) strategy. In spite of the switching noise, the estimation of the rotor position, by a combination of the Slip Frequency PLL and γ - δ Axes Aligner, is of very good quality. However, the speed estimation by the Slip Frequency PLL contains unacceptable noise which must be eliminated by a low pass filter. As the low pass filter introduces time delay, the objective is to find a compensation method.

Low-Pass Filter Design

Fig.3-9 shows the spectrum of the rotor current when the triangle carrier frequency is 2000 Hz. Most of the noise occur at 2kHz. From Fig.3-9, it is reasonable to decide on

500Hz as the cut-off frequency for designing the second order low-pass Butterworth filter [13].

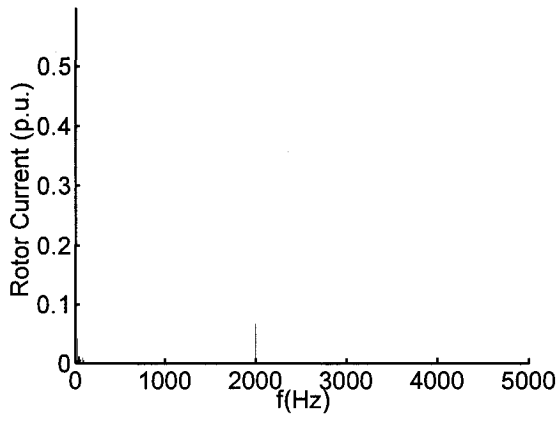


Fig.3-9 FFT of Rotor Current

From the transfer function of the second order low-pass Butterworth filter given as:

$$H_a(s) = \frac{(\Omega_c)^2}{(s - s_0)(s - s_1)}$$
 (3.15)

where Ω_c is cut-off frequency, and the poles are $s_k = \Omega_c \exp(j[\frac{\pi}{2} + (k+0.5)\frac{\pi}{2}])$ k=0,1

The resultant transfer function of the second order low-pass filter is:

$$H_a(s) = \frac{1}{1 + 0.0004504s + 0.000000102s^2}$$
 (3.16)

Speed Measurement with Butterworth Filter

Fig.3-10 compares the estimated speed signal after passing through the Butterworth low-pass filter with the actual rotor speed in an experiment in which the speed of the induction machine is ramped down from super-synchronous speed (slip=-0.1) to subsynchronous speed (slip=0.04).

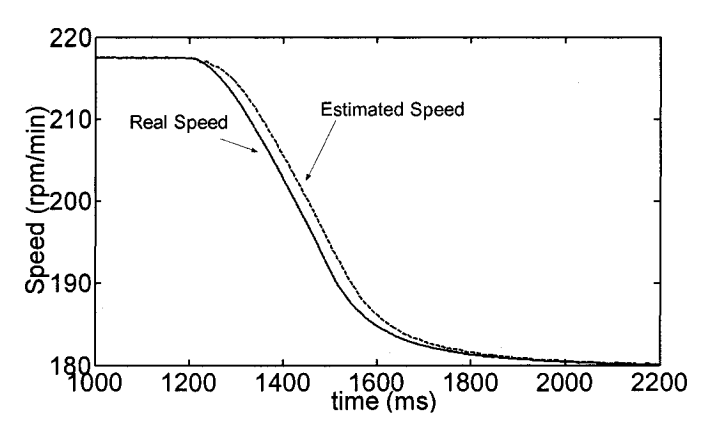


Fig.3-10 Estimated Speed by Using Butterworth Filter

The shortcoming of the low-pass filter is its inherent delay that becomes very apparent in the fast transition from super-synchronous speed to sub-synchronous speed. In the next section, a method will be introduced to compensate it.

3.4.1 Lead-Lag Block Design

As illustrated in Fig.3-11, the 2 time delays: (i) from sensorless method (Slip Frequency PLL) and (ii) from the Butterworth low-pass filter can be added together and compensated by a Lead-Lag Block [14].

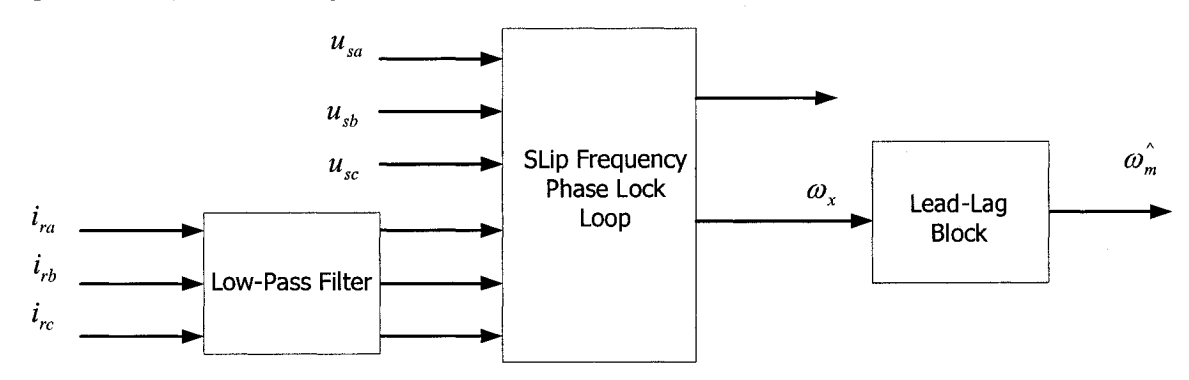


Fig.3-11 Estimating Rotor Speed Diagram

The transfer function of the lead-lag block is given by:

$$H_{lag}(s) = \frac{1 + \alpha_1 s}{1 + \alpha_2 s}$$
 (3.17)

The design values chosen in the example are: $\alpha_1 = 0.1$ and $\alpha_2 = 0.068$

Speed Measurement with Butterworth Filter and Lead-Lag Block

Fig.3-12 shows the experiment of Fig.3-10 with the difference that the Lead-Lag Block is added as shown in Fig.3-11. The time delay in Fig.3-10 has been eliminated by the Lead-Lag compensation.

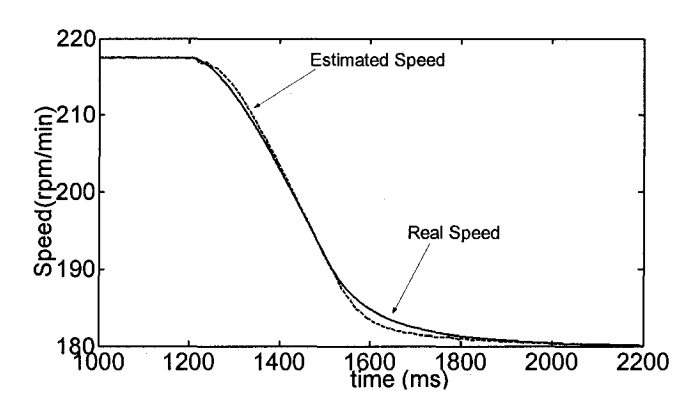


Fig.3-12 Estimated Speed after passing through lagging-leading block

3.5 Conclusion

The chapter has shown that there is a time delay in the speed measurement of the Slip Frequency Phase Lock Loop (PLL). This time delay is related to the time constants $T_R = L_{IR}/R_R$ (associated with the rotor leakage inductance L_{IR} and resistance R_R) and $T_S = L_{IS}/R_S$ (associated with the stator leakage inductance L_{IS} and resistance R_S). The identification of the existence of such time delay as inherent in "sensorless" measurement methods is important from the theoretical foundation viewpoint.

This chapter has identified another source of time delay which will come from the low pass filter needed to remove the switching noise of the Voltage-Source Converters which contaminate the speed measurement from the Slip Frequency Phase Lock Loop (PLL).

This chapter has also shown that the time delays can be compensated by Lead-Lag Blocks.

As the mechanical time constant is very much larger than the electrical time constants, the time delays discussed in this chapter may be of little consequence for most drive applications.

Chapter 4

Sensorless Decoupled P-Q Control for DFIG

4.0 Introduction

As mentioned in the Chapter 1, the doubly-fed induction generator (DFIG) is a very promising candidate for wind turbine application. The DFIG allows the stator to be connected directly to a constant frequency, three-phase grid even though the wind turbine, to which it is coupled, has a variable speed. Variable speed operation is indispensable for optimal wind power acquisition because the DFIG speed must track the changing optimal speed which is a function of the wind velocity as the wind fluctuates in time. The DFIG is economical because when controlled by a Voltage-Source Converter connected to the rotor slip-ring terminals, its MVA rating is reduced by a factor of S_{max} , the maximum slip being $S_{max} \cong 0.3$.

This thesis is oriented towards applying decoupled P-Q control to the DFIG. It is to be recalled that in the $\gamma - \delta$ reference frame, the stator-side real and reactive power are respectively $P_s = v_{sy}i_{sy} + v_{s\delta}i_{s\delta}$ and $Q_s = v_{sy}i_{s\delta} - v_{s\delta}i_{sy}$. When the $\gamma - \delta$ axes are aligned such that $v_{s\delta} = 0$, the stator-side real and reactive power are obtained by controlling the currents $i_{s\delta}$ and $i_{s\delta}$ because $P_s = v_{sy}i_{s\delta}$ and $Q_s = v_{sy}i_{s\delta}$. The challenge in sensorless drive research is to align the $\gamma - \delta$ axes using electrical measurements to estimate mechanical measurements of position and velocity. For this reason, chapter 2 has been devoted to describing the novel sensorless Slip Frequency PLL and the $\gamma - \delta$ Axes Aligner which acquire the mechanical measurements of speed and position.

One criticism of sensorless measurement methods is that they require precise information of the DFIG parameters. For that matter even if the parameters are known precisely, they may change under operation conditions. For example, parameters such as resistances drift with temperature. In chapter 2, sensitivity tests have been performed on the novel sensorless Slip Frequency PLL and $\gamma - \delta$ Axes Aligner. It has been found that they are quite robust. This chapter follows up on this finding and shows how sensorless, *robust*, decoupled P-Q control of the DFIG can be realized.

This chapter incorporates the Slip Frequency PLL, the $\gamma-\delta$ Axes Aligner (of chapter 2) and the Phase Shift Compensation (of chapter 3) to realize decoupled P-Q controller of the DFIG in the system of Fig. 1-1. The rotor side of the DFIG transfers slip power via two back-to-back IGBT Voltage Source Converters (VSCs) to the three-phase ac grid. The two degrees of control of the rotor-side VSC are used to implement the decoupled P-Q control. The Front-End Converter (FEC) operates as a power slack by operating as a DC Voltage Regulator of the dc bus voltage. The second degree of control of the FEC is available to control the reactive power. Both the rotor-side VSC and the FEC have reactive power control capability which can be used to regulate the ac bus voltage or to provide capacitive Var. The many options of Q-control are not pursued in this thesis.

The first section of this chapter will describe the mathematical model of the doubly-fed induction generator (DFIG). The control of decoupled P-Q control of the DFIG is configured with the Slip Frequency PLL and the γ -8 Axes Aligner of chapter 2. The control system is presented in a block diagram. The block diagram shows how the system is simulated by EMTP (R). As already mentioned, the DFIG is represented by the software module of a wound rotor induction machine which is available in EMTP (R). without position sensors will be explained under wind turbine. On the mechanical side of the wound rotor induction machine is T_{mech} , the mechanical torque from the wind turbine driving the induction generator. The author has made use of a software module of a wind turbine which has been developed by Dr. Lianwei Jiao of Tsinghua University [15]. The wind turbine module accepts the wind velocity V_W and the wind turbine speed ω_m as inputs and outputs the wind turbine torque T_{mech} . A section of this chapter is devoted to reviewing the dependence of wind power on turbine speed ω_m and wind velocity V_W . In the last section, it will be shown that the control strategy is inherently robust and an explanation is given for such good fortune.

4.1 Review of Doubly-fed Induction Generator Model

4.1.1 Stationary and Rotating Coordinates

In general, voltages and currents in the 3-phase a-b-c frame can be transformed in the $\alpha-\beta-0$ frame. The zero sequence will be neglected throughout this thesis and hereafter the thesis will only consider the 2-phase $\alpha-\beta$ frame. The relation between the stationary $\alpha-\beta$ coordinate frame and the $\gamma-\delta$ coordinate frame (which is synchronously rotating at the stator angular velocity of $\omega_s(t)$) is illustrated Fig. 4-1. The α -axis is fastened to the stator a-phase. When the rotor speed is $\omega_m(t)$ electrical radian/s, the rotor angle $\theta_r(t)$, between the axes of the stator a-phase and the rotor a-phase is expressed as:

$$\theta_r(t) = \int_0^t \omega_m(t) dt + \theta_r(0) \quad \text{rad.}$$
 (4.1)

Likewise, when the $\gamma - \delta$ coordinates are rotating at an angular velocity ω_s electrical radian/s, then the angle of the angle made between the γ -axis and the α -axis is:

$$\theta_{S}(t) = \int_{0}^{t} \omega_{S} dt + \theta_{S}(0) \quad \text{rad.}$$
 (4.2)

The angles, $\theta_r(0)$ and $\theta_s(0)$, are the initial values of these angles at time t=0 seconds.

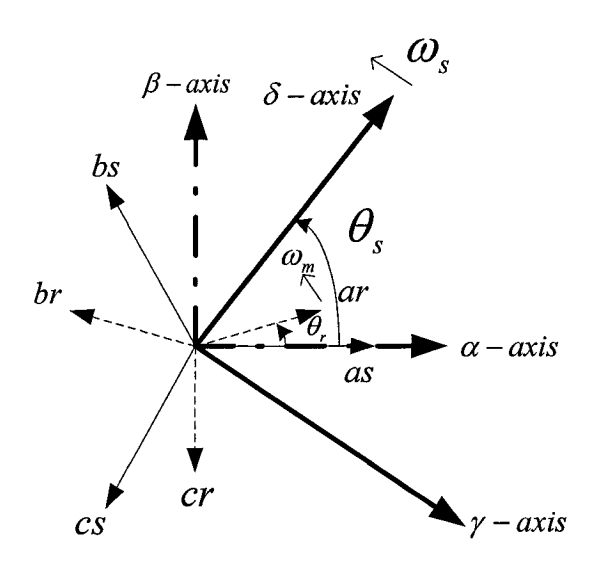


Fig.4-1 Relationship between $\alpha - \beta$ and $\gamma - \delta$ frames

Because the stator voltage vector is aligned with the δ axis, the stator currents $i_{s\gamma}$ and $i_{s\delta}$ control the real power P_S and the reactive power Q_S respectively.

4.1.2 Circuit Model of a Three-Phase Induction Machine

Using the coupled circuit approach and the motor convention, the voltage equations of the magnetically coupled stator and rotor circuits in the original a-b-c frame can be written as follows [16]:

Stator Voltage Equations

$$\underline{y}_{s}^{abc} = \underline{i}_{s}^{abc} R_{s} + d\underline{\lambda}_{s}^{abc} / dt \qquad V$$
 (4.3)

where

$$\underline{v}_{s}^{abc} = (v_{sa}, v_{sb}, v_{sc})^{T}$$

$$\underline{i}_{s}^{abc} = (i_{sa}, i_{sb}, i_{sc})^{T}$$

$$\underline{\lambda}_{s}^{abc} = (\lambda_{sa}, \lambda_{sb}, \lambda_{sc})^{T}$$

Rotor Voltage Equations

$$\underline{v}_{R}^{abc} = \underline{i}_{R}^{abc} R_{R} + d\underline{\lambda}_{R}^{abc} / dt \qquad V$$
 (4.4)

where

$$\underline{v}_{R}^{abc} = (v_{Ra}, v_{Rb}, v_{Rc})^{T}$$

$$\underline{i}_{R}^{abc} = (i_{Ra}, i_{Rb}, i_{Rc})^{T}$$

$$\underline{\lambda}_{R}^{abc} = (\lambda_{Ra}, \lambda_{Rb}, \lambda_{Rc})^{T}$$

Flux Linkage Equations

In matrix notation, the flux linkages of the stator and rotor windings, in terms of the winding inductances and currents, may be written compactly as

$$\begin{bmatrix}
\underline{\lambda}_{s}^{abc} \\
\underline{\lambda}_{R}^{abc}
\end{bmatrix} = \begin{bmatrix}
L_{ss}^{abc} & L_{sR}^{abc} \\
L_{Rs}^{abc} & L_{RR}^{abc}
\end{bmatrix} \begin{bmatrix}
\underline{i}_{s}^{abc} \\
\underline{i}_{R}^{abc}
\end{bmatrix}$$
Weber-turns (4.5)

The submatrices of the stator-to-stator and rotor-to-rotor winding inductances are of the form:

$$L_{SS}^{abc} = \begin{bmatrix} L_{lS} + L_{SS} & L_{Sm} & L_{Sm} \\ L_{Sm} & L_{lS} + L_{SS} & L_{Sm} \\ L_{Sm} & L_{Sm} & L_{lS} + L_{SS} \end{bmatrix}$$
 H (4.6)

$$L_{RR}^{abc} = \begin{bmatrix} L_{lR} + L_{RR} & L_{Rm} & L_{Rm} \\ L_{Rm} & L_{lR} + L_{RR} & L_{Rm} \\ L_{Rm} & L_{Rm} & L_{lR} + L_{RR} \end{bmatrix}$$
H (4.7)

Those of the stator-to-rotor mutual inductances are dependent on the rotor angle, that is

$$L_{SR}^{abc} = [L_{RS}^{abc}]^T = L_{SR} \begin{bmatrix} \cos\theta_r & \cos(\theta_r + 2\pi/3) & \cos(\theta_r - 2\pi/3) \\ \cos(\theta_r - 2\pi/3) & \cos\theta_r & \cos(\theta_r + 2\pi/3) \\ \cos(\theta_r + 2\pi/3) & \cos(\theta_r - 2\pi/3) & \cos\theta_r \end{bmatrix}$$
(4.8)

where L_{lS} is the per phase stator winding leakage inductance, L_{lR} is the per phase rotor winding leakage inductance, L_{sm} =-0.5 L_m is the mutual inductance between stator windings, L_{Rm} =-0.5 L_m is the mutual inductance between rotor windings, and L_{SS} L_{RR} = L_{SR} = L_m . (L_{SS} + L_{lS}) is the self-inductance of the stator winding and (L_{RR} + L_{lR}) is the self-inductance of the rotor winding,

According to the above equations, the idealized machine is described by six first-order differential equations, one for each winding. These differential equations are coupled to one another through the mutual inductance between the windings. In particular, the stator-to-rotor coupling terms are a function of rotor position; thus, when the rotor rotates, these coupling terms vary with time. It is convenient to transform the six equations with time-varying inductances to other six equations with constant inductances by using the a-b-c to $\gamma - \delta - 0$ mathematical transformation.

4.1.3 Machine Model in $\gamma - \delta - 0$ Reference Frame

As the idealized three-phase induction machine has a uniform airgap, there is no difficulty in transforming the a-b-c equations to a new set in the $\gamma - \delta - 0$ frame which rotates at the speed ω_s of the stator magnetic flux.

$\gamma - \delta - 0$ Voltage Equations

The stator winding a-b-c voltage equation, expressed as (4.3), is transformed to the $\gamma - \delta - 0$ frame as:

$$\underline{\underline{v}}_{s}^{\gamma\delta0} = \omega_{s} \begin{bmatrix} 0 & 1 & 0 \\ -1 & 0 & 0 \\ 0 & 0 & 0 \end{bmatrix} \underline{\underline{\lambda}}_{s}^{\gamma\delta0} + d\underline{\underline{\lambda}}_{s}^{\gamma\delta0} / dt + \underline{R}_{s}^{\gamma\delta0} \underline{\underline{i}}_{s}^{\gamma\delta0}$$
 (4.9)

where

$$\underline{R}_{s}^{\gamma\delta0} = R_{s} \begin{bmatrix} 1 & 0 & 0 \\ 0 & 1 & 0 \\ 0 & 0 & 1 \end{bmatrix}$$

Likewise, the rotor quantities must be transferred onto the same $\gamma - \delta$ frame. As we have done with the stator voltage equations, we obtain the following $\gamma - \delta - 0$ voltage equations for the rotor windings:

$$\underline{\underline{v}}_{r}^{\gamma\delta0} = (\omega_{s} - \omega_{r}) \begin{bmatrix} 0 & 1 & 0 \\ -1 & 0 & 0 \\ 0 & 0 & 0 \end{bmatrix} \underline{\underline{\lambda}}_{R}^{\gamma\delta0} + d\underline{\underline{\lambda}}_{R}^{\gamma\delta0} / dt + \underline{R}_{R}^{\gamma\delta0} \underline{i}_{R}^{r\delta0}$$
 (4.10)

where

$$\underline{R}_{R}^{\gamma\delta 0} = R_{R} \begin{bmatrix} 1 & 0 & 0 \\ 0 & 1 & 0 \\ 0 & 0 & 1 \end{bmatrix}$$

$\gamma - \delta - 0$ Flux Linkage Relation

The stator and rotor flux linkage relationships can be expressed compactly as

$$\begin{bmatrix} \lambda_{s\gamma} \\ \lambda_{s\delta} \\ \lambda_{s0} \\ \lambda_{R\gamma} \\ \lambda_{R\delta} \\ \lambda_{R0} \end{bmatrix} = \begin{bmatrix} L_s & 0 & 0 & L_m & 0 & 0 \\ 0 & L_s & 0 & 0 & L_m & 0 \\ 0 & 0 & L_{ls} & 0 & 0 & 0 \\ L_m & 0 & 0 & L_R & 0 & 0 \\ 0 & L_m & 0 & 0 & L_R & 0 \\ 0 & 0 & 0 & 0 & 0 & L_{lR} \end{bmatrix} i_{s\delta} i_{s0} i_{R\gamma}$$

$$(4.11)$$

where

$$L_s = L_{ls} + L_m$$
$$L_R = L_{lR} + L_m$$

In summary, a set of voltage-current differential equations of two-pole doubly-fed induction machine on the $\gamma - \delta$ coordinates is shown as following [10]:

$$\begin{pmatrix} v_{s\gamma} \\ v_{s\delta} \\ v_{R\gamma} \\ v_{R\delta} \end{pmatrix} = \begin{pmatrix} R_s + \frac{d}{dt} L_s & -\omega_s L_s & \frac{d}{dt} L_m & -\omega_s L_m \\ \omega_s L_s & R_s + \frac{d}{dt} L_s & \omega_s L_m & \frac{d}{dt} L_m \\ \frac{d}{dt} L_m & -(\omega_s - \omega_m) L_m & R_R + \frac{d}{dt} L_R & -(\omega_s - \omega_m) L_m \\ (\omega_s - \omega_m) L_m & \frac{d}{dt} L_m & (\omega_s - \omega_m) L_R & R_R + \frac{d}{dt} L_R \end{pmatrix} \begin{pmatrix} i_{s\gamma} \\ i_{s\delta} \\ i_{R\gamma} \\ i_{R\delta} \end{pmatrix}$$

$$(4.12)$$

From the above matrix equations, the equivalent circuit shown in Fig. 9 can be derived.

$\gamma - \delta - 0$ Torque Equation

The electromechanical torque developed by the machine is given as:

$$T_{em} = \frac{p}{2} (\lambda_{s\gamma} i_{s\delta} - \lambda_{s\delta} i_{s\gamma})$$

$$= \frac{p}{2} L_m (i_{R\gamma} i_{s\delta} - i_{R\delta} i_{s\gamma}) \quad \text{N.m.}$$
(4.13)

where p is the number of poles.

The mechanical equation of motion of the motor is obtained by equating the inertia torque to the accelerating torque, that is

$$J\frac{d\omega_m}{dt} = T_{em} + T_{mech} - T_{damp} \qquad \text{N.m.} \quad (4.14)$$

 T_{em} is the electromechanical torque of (4.13) of the DFIG. T_{damp} is the damping torque and the negative sign is to indicate that it acts in the direction opposite to rotation. In wind turbine generation application, the positive wind turbine torque T_{mech} accelerates the rotor until it meets an equal and opposite counter torque T_{em} of the DFIG. The operating speed is determined by the decoupled P-Q controller which produces the requisite T_{em} such that $T_{em} + T_{mech} - T_{damp} = 0$ at the operating speed.

4.2 Wind Turbine Model

The research has made use of a software module of the wind turbine which has been developed by Dr. Lianwei Jiao of Tsinghua University. The wind turbine module is coupled to the wound-rotor induction machine module in EMTP (R). This section contains the technical background of the wind turbine model.

The product of wind turbine torque T_{mech} and rotor speed ω_m is the wind turbine power $P_t = T_{mech}\omega_m$.

From [17], the amount of power (P_t) capable of being produced by a wind turbine is given by

$$P_{t} = \frac{1}{2} \rho \pi r^{2} C_{p}(\lambda) v_{w}^{3}$$
 (4.15)

where

 ρ is the air density

 C_p is the power coefficient of the wind turbine

 v_{w} is the wind velocity

r is the turbine rotor radius

 C_p is dependent on the ratio between the tangential velocity of the blade tip $(R \cdot \omega_m \cdot gear_ratio)$ and the wind velocity (v_w) . This ratio, known as the tip-speed ratio, is defined as

$$\lambda = \frac{\omega_m \cdot r}{v_{yy}} gear_ratio \tag{4.16}$$

where

 ω_m is the angular velocity of the DFIG r is the radius of the turbine v_w is the wind velocity

Fig.4-2, taken from [18], shows a typical relationship between C_p and the tip-speed ratio λ for a given pitch angle. In this thesis, it is assumed that the pitch angle remains fixed. From the C_p -vs- λ curve of Fig. 4-2, (4.15), (4.16) and a knowledge of the gear ratio relating the turbine speed and the DFIG speed, one can construct the P_t -vs- ω_m curves of Fig. 4-3 for a family of wind velocities v_w .

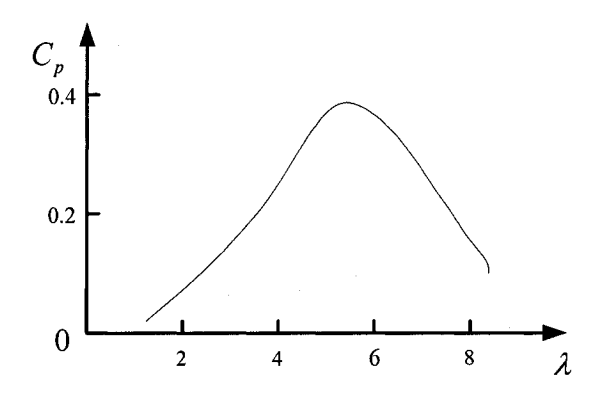


Fig.4-2 Power coefficient as a function of tip speed ratio

Fig. 4-3 shows a P_{max} -vs- ω_m curve which passes through the peaks of P_t -vs- ω_m curves for each wind velocity V_w . The P_{max} -vs- ω_m curve corresponds to the maximum point $(C_{p_{max}}, \lambda_{max})$ in Fig. 4-2. In order to maximize the output power of generator, it is desirable that the DFIG is controlled so that at each rotor speed ω_m , it is made to output a power corresponding to the value in the P_{max} -vs- ω_m curve in Fig.4-3 [15]. Under such

control, the DFIG would produce a counter-torque $T_{em} = P_{max}/\omega_m$ to match the turbine torque T_{mech} . This means that in (4-14), $T_{em} + T_{mech} - T_{damp} = 0$.

Since $P_s = v_{sy}i_{s\delta}$ and $Q_s = v_{sy}i_{s\delta}$ in decoupled P-Q control refers to complex power at the stator side terminals, one is reminded that the rotor delivers slip power (sP_{max}) by way of the back-to-back VSCs (see Fig. 1-1). As the slip is $s=(1-\omega_m/\omega_S)$, it follows that the stator power reference, P_{s-ref} , of the decoupled P-Q control be programmed to assign P_{s-ref} -vs- ω_m characteristics where P_{s-ref} = $P_{max}\omega_m/\omega_S$. Fig.4-3 illustrates the P_{s-ref} -vs- ω_m characteristics graphically.

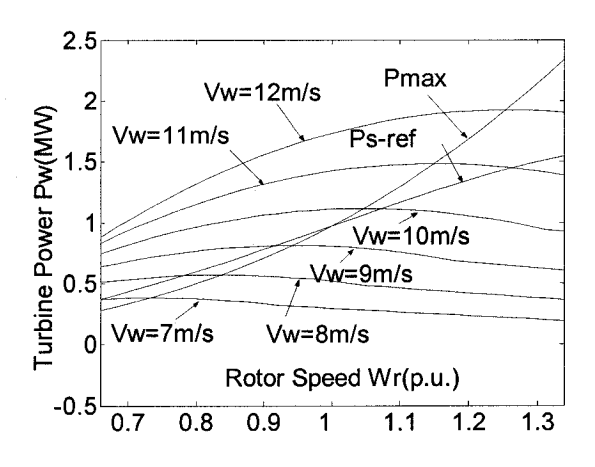


Fig. 4-3 Wind Power-vs-rotor speed

4.3 Control of Rotor Side Converter (VSC)

The block diagram of the proposed decoupled P-Q control of the rotor side VSC is shown in Fig.4-4. Following in the footsteps of [8,9], for a specification of the stator-side complex power as inputs, the outputs of Fig.4-4 are the rotor voltages (v_{ra} , v_{rb} , v_{rc}) which are the modulating signals of the SPWM control of the rotor-side VSC.

Explanation of the operation of the decoupled P-Q control is given block by block.

Phase Mixers

As mentioned in chapter 2, the Phase Mixer of Fig.3-2 (b) can be used to add or subtract the phases $(\omega_S t + \delta_S)$ and $(\Phi + \omega_X t + \delta_X)$ which have been extracted by the Slip

Frequency PLL and the γ - δ Axes Aligner Block. Such operations are equivalent to making transformations from one reference frame to another.

Thus the lower pair of Phase Mixers transform the rotor currents i_{ra} , i_{rb} , i_{rc} in the a-b-c frame to $i_{R\gamma}$, $i_{R\delta}$ in the 2-phase γ - δ frame. Likewise, the upper of Phase Mixers transform the voltage references $v^*_{R\gamma}$, $v^*_{R\delta}$ in the γ - δ frame to v^*_{ra} , v^*_{rb} , v^*_{rc} in the a-b-c frame. Note that asterisks * are used to denote reference values.

The references for the rotor currents $i_{R\gamma}^*$ and $i_{R\delta}^*$ are derived from the active and reactive power references P_s^* and Q_s^* respectively.

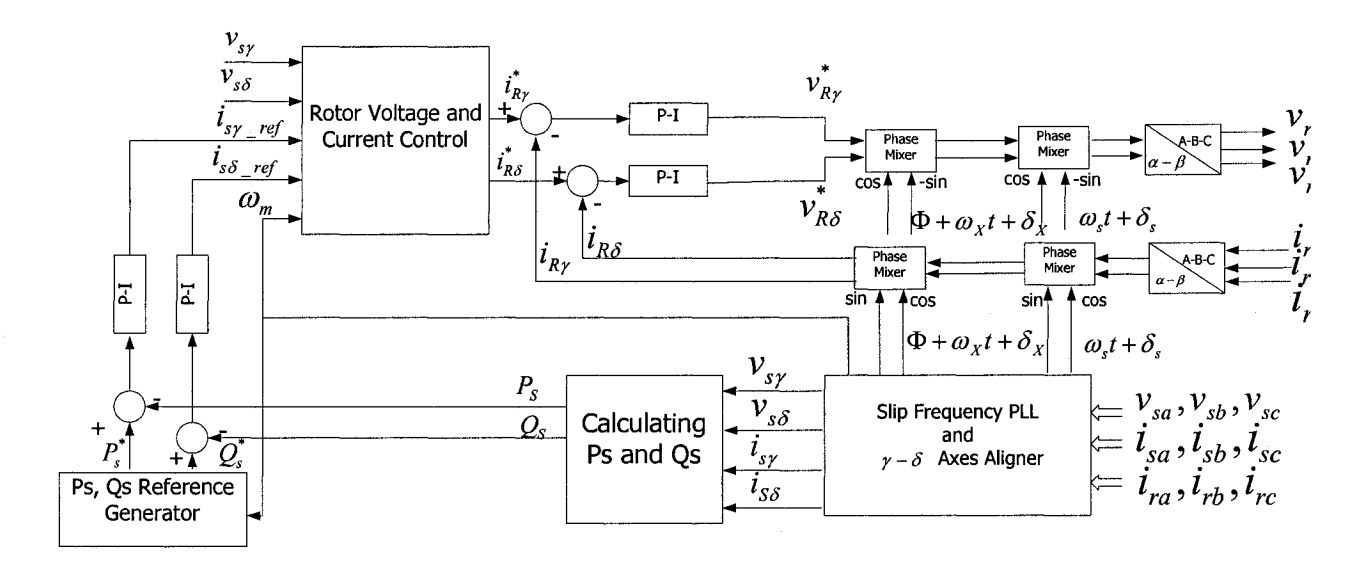


Fig.4-4 Block diagram of rotor side VSC control

4.3.1 Slip Frequency PLL and $\gamma - \delta$ Axes Aligner Block

This block contains the Slip Frequency PLL of Fig.2-2 and the $\gamma - \delta$ axes Aligner of Fig.2-4. Its inputs are the stator voltages v_{sa}, v_{sb}, v_{sc} , the stator currents i_{sa}, i_{sb}, i_{sc} and the rotor currents i_{ra}, i_{rb}, i_{rc} . Its outputs are the estimated rotor position $(\Phi + \omega_X t + \delta_X)$, and the rotor speed ω_{m} . By applying the estimated position, the rotor currents and voltages can be transformed into the same $\gamma - \delta$ frame of the stator. It then computes $(i_{s\gamma}, i_{s\delta}, v_{s\gamma}, v_{s\delta})$ which are used in the P_S and Q_S Computation Block. P_S and Q_S are the feedback complex

power components. Inside the Slip Frequency PLL, there is another PLL which measures the phase $(\omega_S t + \delta_S)$.

4.3.2 P_s and Q_s Reference Generator Block

Fig. 4-5 (a) shows the detail of the P_s^* Reference Generator of Fig. 4-4. The $P_{S-ref^*}vs$ - ω_m curve of Fig. 4-3 is programmed in a Lookup Table. Corresponding to the rotor speed ω_m measured by the Slip Frequency PLL, it outputs the reference stator power reference P_s^* .

This thesis has not investigated on how the reactive power should be controlled. This will be a good topic for future research. For the present, it is assumed that a reference Q_S^* will be set for a rotor speed ω_m .

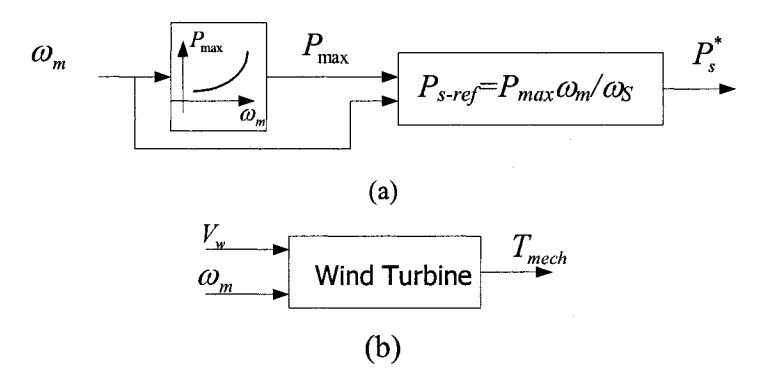


Fig.4-5 (a) P_s reference generator (b) T_{mech} generator

On the subject of Lookup Table, this is a good place to point out that the wind turbine has a wind torque which appears as T_{mech} in (4-13) and T_{mech} is obtained from another Lookup Table. The simulation software of the DFIG of EMTP(R) has a port for inputting T_{mech} . T_{mech} in turn is the output of a black-box whose inputs are the wind velocity V_W and rotor speed ω_m as shown in Fig. 4-5 (b). The black-box has the C_p -vs- λ curve of Fig. 4-2 programmed in a Lookup Table. For inputs V_W and rotor speed ω_m , λ is computed from (4.16). The corresponding $C_p(\lambda)$ is read from the Lookup Table. From (4.15), the wind-turbine power P_t is available and the output $T_{mech} = P_t/\omega_m$.

4.3.3 P_s and Q_s Computation Block

The inputs of the block are $i_{s\gamma}$, $i_{s\delta}$, $v_{s\gamma}$, $v_{s\delta}$ which come from the Slip Frequency PLL and $\gamma - \delta$ axes Aligner block. Since $v_{s\delta} = 0$, $P_s = v_{s\gamma}i_{s\gamma}$ and $Q_s = v_{s\gamma}i_{s\delta}$ are calculated in this block. The measurements P_s and Q_s are used as feedback signals.

4.3.4 Negative Feedback of Complex Power

The errors $\varepsilon_p = P_s^* - P_s$ and $\varepsilon_Q = Q_s^* - Q_s$, after passing through P-I (proportional integral) blocks, are taken as the current references $i_{s\gamma}^*$ and $i_{s\delta}^*$ in the outer feedback loop. This is valid since $v_{s\delta} = 0$ and the voltage $v_{s\gamma}$ is merged with the proportionality constants of the P-I blocks.

4.3.5 Rotor Voltage and Current Control Block

This block accepts the stator current references $i_{s\gamma}^*, i_{s\delta}^*$ and the stator voltages $v_{s\gamma}, v_{s\delta}$ as inputs and outputs the rotor-side current references $i_{R\gamma}^*, i_{R\delta}^*$. The outputs are based on the first two rows of (4.14) with the assumption that the d_/dt_terms are zero. The rotor-side current references $i_{R\gamma}^*, i_{R\delta}^*$ are:

$$\begin{pmatrix}
i_{Ry}^{*} \\
i_{s\delta}^{*}
\end{pmatrix} = \begin{pmatrix}
(v_{s\delta} - \omega_{s}L_{s}i_{sy}^{*} - R_{s}i_{s\delta}^{*}) / \omega_{s}L_{m} \\
(-\omega_{s}L_{s}i_{s\delta}^{*} + R_{s}i_{sy}^{*}) / \omega_{s}L_{m}
\end{pmatrix} (4.17)$$

Rotor Current Tracking:

From 4.17, it is clear that it is possible to achieve robust control by using the rotorside VSC to operate as a rotor current tracker. The reference current vector $[i_{R\gamma}^*, i_{R\delta}^*]^T$ is only dependent on parameters $\omega_S L_S$, $\omega_S L_m$ and R_S . Furthermore, since $\omega_S L_S \approx \omega_S L_m$ and $R_S/\omega_S L_m \approx 0$, it is expected that decoupled P-Q control can be implemented in spite of inaccuracies in the stator resistance R_S and the stator leakage inductance L_{IS} . Because the other parameters, the rotor resistance R_R and the rotor leakage inductance L_{IR} , do not enter into the picture, the decoupled P-Q control by current track is not sensitive to their variation also.

As illustrated in Fig. 4-4, the current tracking is accomplished by negative feedback. The feedback current vector is $[i_{R\gamma},i_{R\delta}]^T$. The errors $\varepsilon_{R\gamma}=(i_{R\gamma}^*-i_{R\gamma})$ and $\varepsilon_{R\delta}=(i_{R\delta}^*-i_{R\delta})$ after passing through P-I blocks, form $v_{R\gamma}^*$ and $v_{R\delta}^*$. Note that the gains, notably the integral gain in the P-I blocks, will ensure that $v_{R\gamma}^*$ and $v_{R\delta}^*$ will be high enough to null the errors $\varepsilon_{R\gamma}$ and $\varepsilon_{R\delta}$ so that the rotor current vector $[i_{R\gamma},i_{R\delta}]^T$ tracks the reference vector $[i_{R\gamma}^*,i_{R\delta}^*]^T$.

The feedback rotor current vector $[i_{R\gamma}, i_{R\delta}]^T$ has to be transformed from the a-b-c frame to the γ - δ frame. Likewise, the command voltage vector $[v_{R\gamma}^*, v_{R\delta}^*]^T$ in the γ - δ frame has to be transformed to the a-b-c frame to control each phase voltage of the VSC.

4.4 Control of Front End Converter (Stator Side Converter)

The function of the Front End Converter (Stator Side Converter) is to provide a path for the rotor slip power of the DFIG to and from the ac grid. As the magnitude and the direction of slip power changes with the operating slip, this VSC must rectify or invert the right amount of power to keep the power balance in the dc link. As is well known, this power slack property is built into the VSC by configuring the real power control to regulate the dc link voltage.

The dc link consisting of back-to-back converters, consisting of the Rotor-Side VSC and Front End Converter, is well known and is not part of the research of this thesis. Nevertheless, it is included in this chapter because designing it is part of the educational experience of a master student. In order to broaden the learning experience, the hysteresis current control method is adopted. As is well known, hysteresis current control is simple

to implement and it has fast response. As shown in [19], it is capable of: 1) unity and even leading power factor, 2) bilateral power transfer.

4.4.1 Hysteresis Current Control

Before proceeding to 3-phase Hysteresis Current Control, the single phase bridge converter, which has sufficient simplicity, is used to explain the operation of Hysteresis Current Control. Fig.4-6 shows the schematic in which the solid-state switches VU and VL are triggered ON and OFF complementarily by logic signals from the Hysteresis Current Control Logic Block. The inputs of the Control Logic are: the reference signal $i_R(t)$, the tolerance band h and measured value of $i_R(t)$.

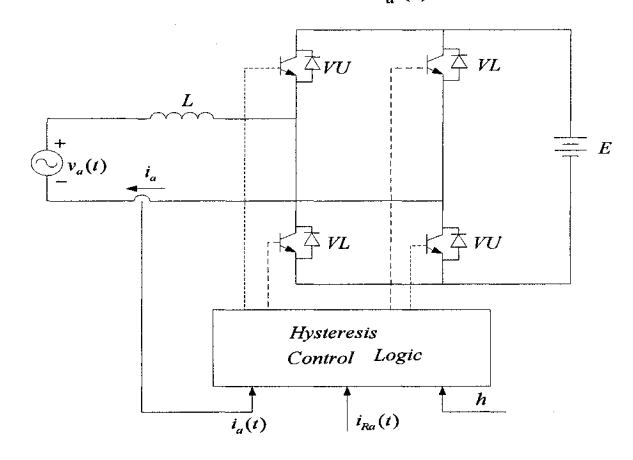


Fig.4-6 Single Phase hysteresis current controlled converter

Switching Function

The switching states of power electronics valves VU and VL are described by the switch function S_a which assumes the values of:

 $S_a = +1$ when VU is switched ON and VL is switched OFF

 $S_a = -1$ when VU is switched OFF and VL is switched ON

The switch function allows for two possible polarities of the applied dc voltage E to be applied to the loop consisting of the ac source v_a and the inductance L in the ac-side. From the kirchhoff's Voltage Law, one has the equation by which the current i_a can be solved for the two switching states.

$$L\frac{di_a}{dt} = v_a - S_a E \tag{4.18}$$

The solution is:

$$i_a(t) = i_a(t_0) + \int_{t_0}^{t} \frac{v_a(t) - S_a E(t)}{L} dt$$
 (4.19)

Current Gradients

From (4.18) the current gradient is defined as follows:

$$\frac{di_a}{dt} = \frac{v_a - S_a E}{L} \tag{4.20}$$

Fig. 4-7 [20] shows broken lines which join the trajectories of possible solutions of (4-20) for S_a =+1 and S_a =-1. They have the gradients defined by (4.20).

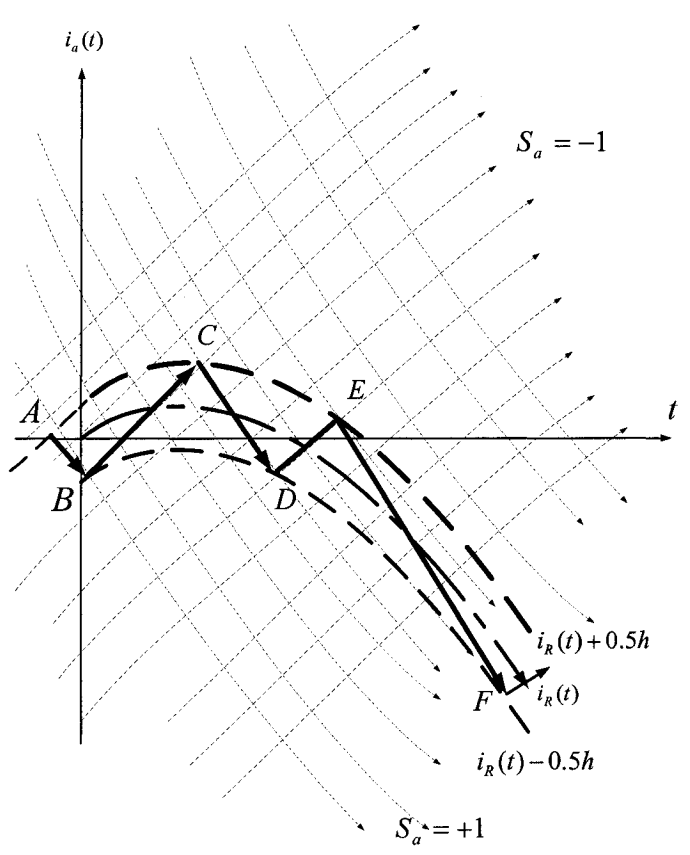


Fig.4-7 $i_a(t)$ tracks reference current $i_R(t)$ within the tolerance band h

In Fig. 4-6, E has been assumed to be a constant value with E> $|v_a(t)|$, and $v_a(t)$ is a sinusoidally time varying function. In a general way, the current i_a follows the trajectory of the solution of either S_a=1 or -1. One can use portions of two families of curves to approximate any desired waveform $i_R(t)$ within a tolerance of $\pm 0.5h$ where h is tolerance bandwidth. The switching is activated by the Hysteresis Control Logic when i_a crosses the bounds defined by $i_R(t) \pm 0.5h$.

As illustrated in Fig.4-7, starting at $i_a(t)=0$, by switching state $S_a=-1$, the current grows along BC. When it exceeds the Upper Bound defined as $i_R(t)+0.5h$, the switching state is changed to $S_a=+1$. The current follows the trajectory of $S_a=+1$ along CD until it reaches the Lower Bound defined as $i_R(t)-0.5h$. At D, the switching state is changed to Sa=-1 and again the ascending trajectory is followed. Thus by alternately switching to and from $S_a=+1, S_a=-1$, the current is kept within the upper and lower bounds. When h is made small, the approximation to $i_R(t)$ improves at the expense of fast switching rates.

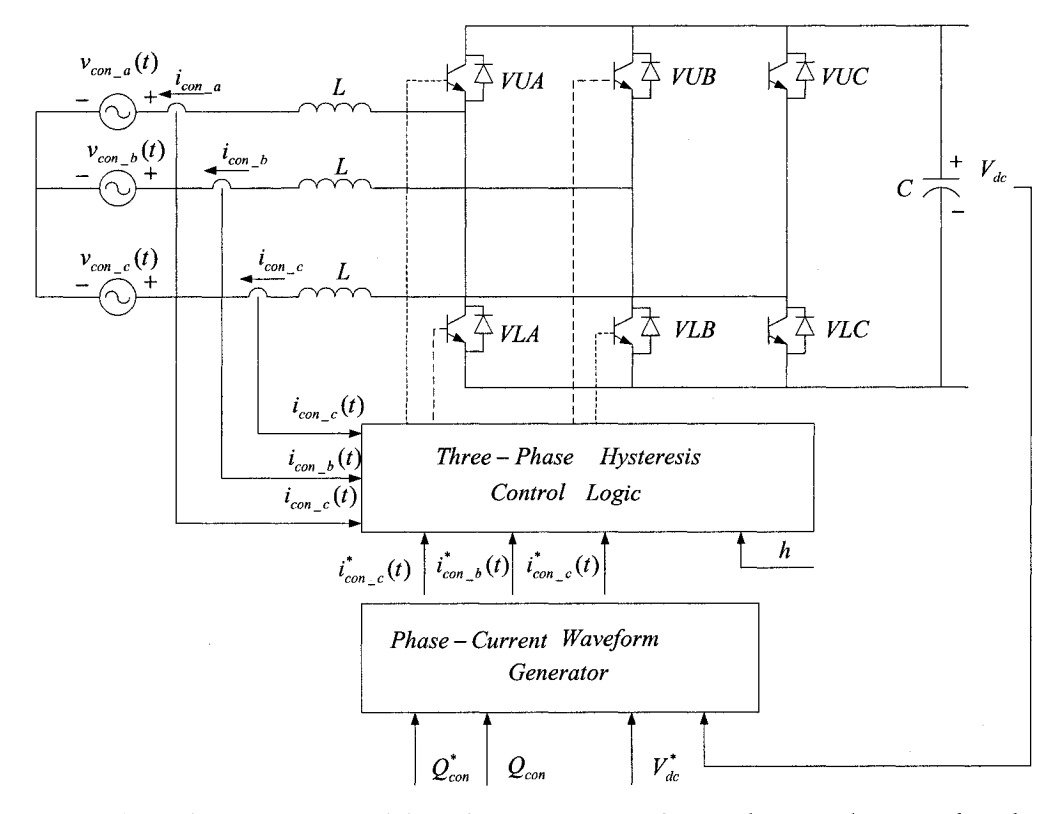


Fig. 4-8 Three-phase converter with inner hysteresis current loop and outer voltage regulator loop

So far, one has reviewed the properties of the single-phase hysteresis control. The single-phase hysteresis current control is extended to three-phase hysteresis current control shown in Fig.4-8. The measured 3-phase as currents $i_{con_a}(t), i_{con_b}(t), i_{con_c}(t)$ compared with the reference are currents $(i_{con_a}^*(t), i_{con_b}^*(t), i_{con_c}^*(t))$ respectively and are made to track the references when the resulting errors cross the hysteresis-band defined by "h" in the manner described by the example of the single-phase converter.

Control of the real power P and the reactive power Q of the FEC is based on designing negative feedback control in which the measured complex power components P and Q are compared to the references P_{con}^* and Q_{con}^* and using the reference currents $(i_{con_a}^*(t), i_{con_b}^*(t), i_{con_c}^*(t))$ to null the errors P_{con}^* -P and Q_{con}^* -Q.

Q control is not the subject of this thesis. The control of the FEC is configured to regulate the DC link voltage and this makes it operate as a power slack. The dc link voltage V_{dc} is measured and compared to the reference DC voltage V_{dc}^* . The error $V_{dc}^* - V_{dc}$ is applied to P_{con}^* in negative feedback to null the error.

4.4.2 DC Voltage Regulator

As illustrated in Fig.4-9, the terminal AC voltage ($v_{con_a}, v_{con_b}, v_{con_c}$) and currents ($i_{con_a}, i_{con_b}, i_{con_c}$) are measured and transformed into $v_{con_\gamma}, v_{con_\delta}, i_{con_\gamma}, i_{con_\delta}$ by transformation from the a-b-c frame to the γ - δ frame. There are 2 nested feedback loops.

The inner feedback ensures that the measured active power P_{con} tracks the reference P_{con}^* . The measured active power P_{con} is obtained by using the equation $P_{con} = (v_{con_\gamma}i_{con_\gamma} + v_{con_\delta}i_{con_\delta})$. The error with respect to the reference active power P_{con}^* , after passing through the proportional and integral control blocks, is applied to the converter current references $i_{con_\gamma}^*$. After reference frame transformation from the γ - δ

frame to the a-b-c frame, $i_{con_{-}\gamma}^{*}$ becomes the reference current $(i_{con_{-}a}^{*}(t), i_{con_{-}b}^{*}(t), i_{con_{-}c}^{*}(t))$ of Hysteresis Current Control.

When decoupled P-Q control is also applied to the FEC, the 2 nested controls can be merged into one. This is by omitting the inner real power regulation loop. This is because $P_{con} = v_{con_{-}\gamma}i_{con_{-}\gamma}$ and it is sufficient to apply the dc voltage error directly to $i_{con_{-}\gamma}^{*}$ as shown in Fig. 4-9 (a).

By nulling the DC voltage error, the DC voltage regulator sends or absorbs the right amount of real power to balance the system demand so that its capacitors can be kept charged at V_{dc}^* . Thus the DC voltage regulator is a power slack.

This thesis has not treated Q-control of the FEC. Q-control, if required, is obtained using the block diagram of Fig. Fig. 4-9 (b).

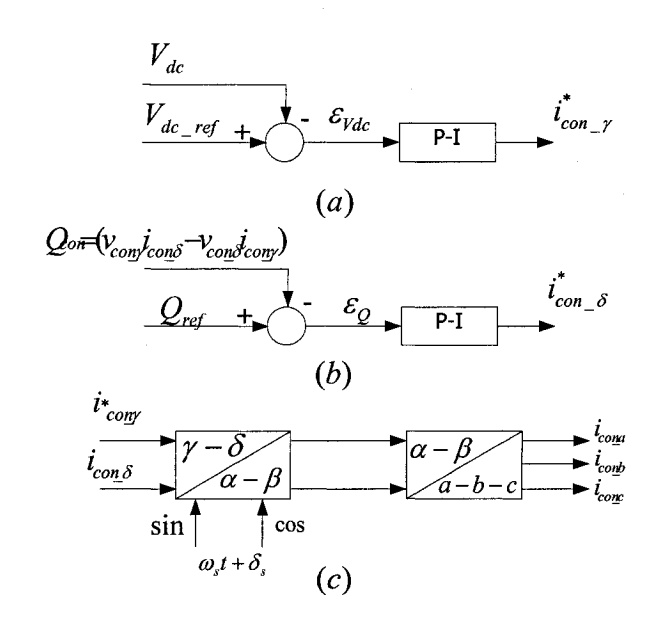


Fig.4-9 The outer-Loop (Phase-Current Generator)
(a) DC Voltage Control
(b) Q Control
(c) Current Transformation From $\gamma - \delta$ frame to a-b-c frame

4.4.3 Simulation test of DC Voltage Regulator

In the test of the Front End Converter with the DFIG control, the reference value of V_{dc} is set as 1500V and the reference value of the reactive power Q_{con}^* =0.00 p.u. The schematic and parameters used for the simulation are listed in Appendix A.

Fig.4-10 shows the system response to a step change in which V_{dc}^* is changed from 1500v to 1550v. The simulation Fig. 4-10 (a) shows fast response in V_{dc} that settles to the desired value in 0.01 second. Fig. 4-10 (b) shows the P_{con} and Q_{con} during this transient.

Fig.4-11 is a test to show that the Front End Converter (stator-side converter) automatically conveys the slip power of the rotor output. In the test, the DFIG runs from super-synchronous speed to sub-synchronous speed as shown in Fig.4-11 (a). Fig.4-11 (b) shows the reversal of real power from -0.07p.u to 0.05 p.u. This "power slack" capability is made possible by regulating the dc voltage which as shown in Fig.4-11 (c) is maintained roughly constant.

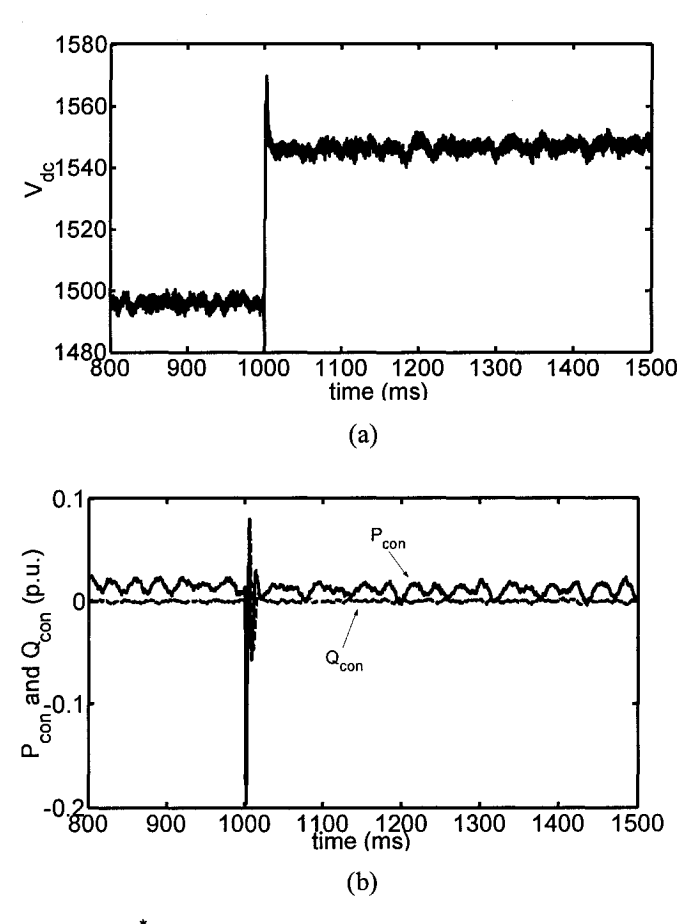
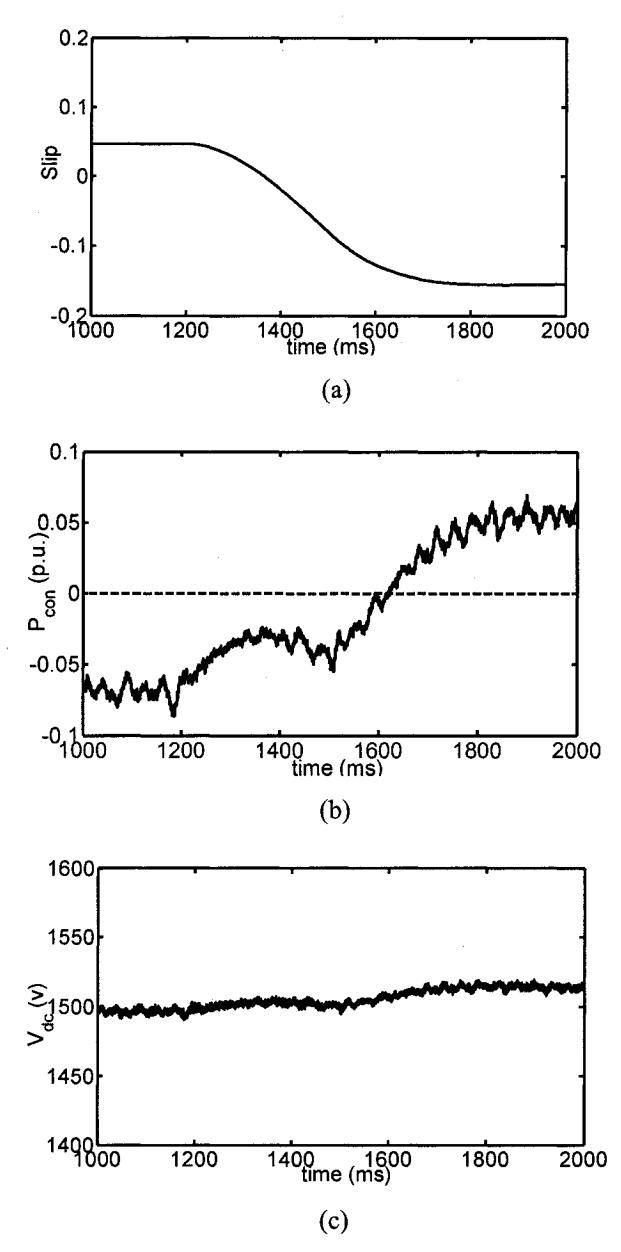


Fig.4-10 Step change of V_{dc}^* from 1500 V to 1550 V at t=1000ms (a) V_{dc} (b) P_{con} and Q_{con}



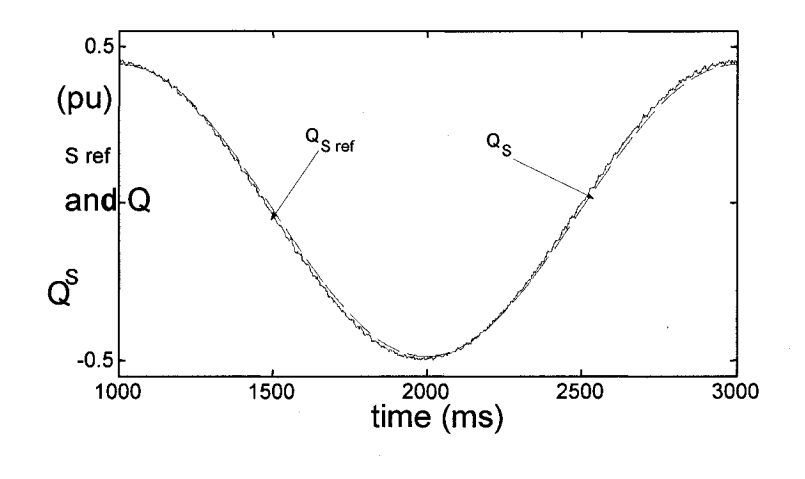
4.5 Simulation tests on DFIG

The simulation tests have been tested on the software module of a slip-ring induction machine of EMTP (R) which is used to represent the DFIG of this thesis. The parameters of the 1 MW DFIG are taken from [21] and are listed in Appendix A.

4.5.1 Static simulation tests of sensorless decoupled P-Q control

Fig.4-12 shows the simulation results of static tests in which the rotor speed is held constant. The reactive power reference $Q_{S \ ref}$ is given a sinusoidal variation. The real power reference $P_{S \ ref}$ is held constant so that it is easy to see if the Q-control couples on to the P-control. How well the sensorless control of Fig.4-12 succeeds in implementing decoupled P-Q control can be seen in how closely the simulated values of Q_s and P_s overlap their references Q_{sref} and P_{sref} .

In Fig.4-12, the simulations are for the case in which the parameters entered in the control blocks correspond exactly to the parameters of the DFIG listed in Appendix A. Fig. 4-12 is used as the benchmark in the tests (Fig.4-13 to 4-15) on robustness.



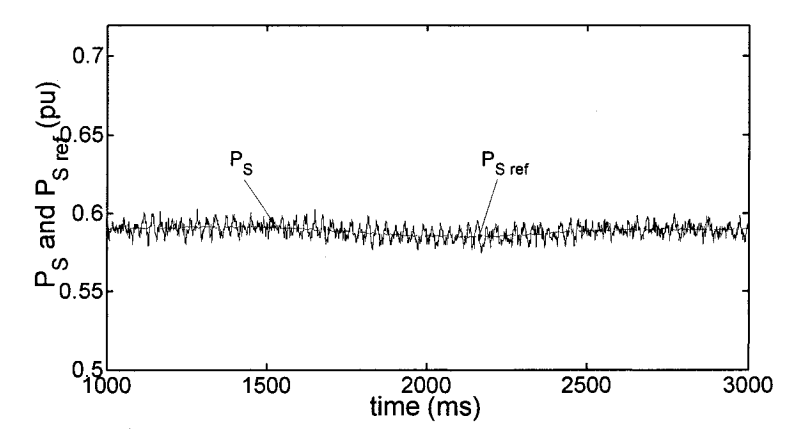


Fig. 4-12 Simulation of DFIG: Qs _{ref} variable, Ps _{ref}=constant

(a) Qs _{ref} and measured Qs

(b) Ps _{ref} and measured Ps

4.5.2 Test on Robustness

In Chapter 2, it has already been shown that the Slip Frequency PLL and γ - δ Axes Aligner together offer robust estimation of rotor position. The motivation of this section is to verify that the decoupled P-Q control can also be made robust by making the rotor VSC operate as a current tracker. Three simulation case studies, concerning R_s , L_{ls} and L_m , will be presented below to give assessments of the claims to robustness of the control.

4.5.2.1 Stator Resistor Uncertainty-- R_s

The first source of uncertainty is that the parameters have been measured inaccurately. The second source is that the resistor values may vary with changes in temperature. It means that the stator and rotor resistors have different values according to different working conditions. In general, the stator resistance is small compared with the magnetizing reactance. For instance, when we can neglect the stator resistance and with $v_{s\delta} = 0$, the rotor current references are:

$$\begin{pmatrix}
i_{R\gamma}^{*} \\
i_{R\delta}^{*}
\end{pmatrix} \approx \begin{pmatrix}
(-\omega_{s}L_{s}i_{s\gamma}^{*}) / \omega_{s}L_{m} \\
(-v_{s\gamma} - \omega_{s}L_{s}i_{s\delta}^{*}) / \omega_{s}L_{m}
\end{pmatrix} \tag{4.21}$$

which are substantially the same numerically as in (4.17).

This is borne out by Fig.4-13 (a) and (b) which show the simulation results when in the controls of Fig. 4-4 the stator resistance is set to R_s =0 (based on the same test setup as in section 4.5.1). The DFIG retain the parameters of Appendix A. As Q_s and P_s overlap their references Q_{sref} and P_{sref} , it is clear that the parameter R_s has very little effect on the ability to implement decoupled P-Q control.

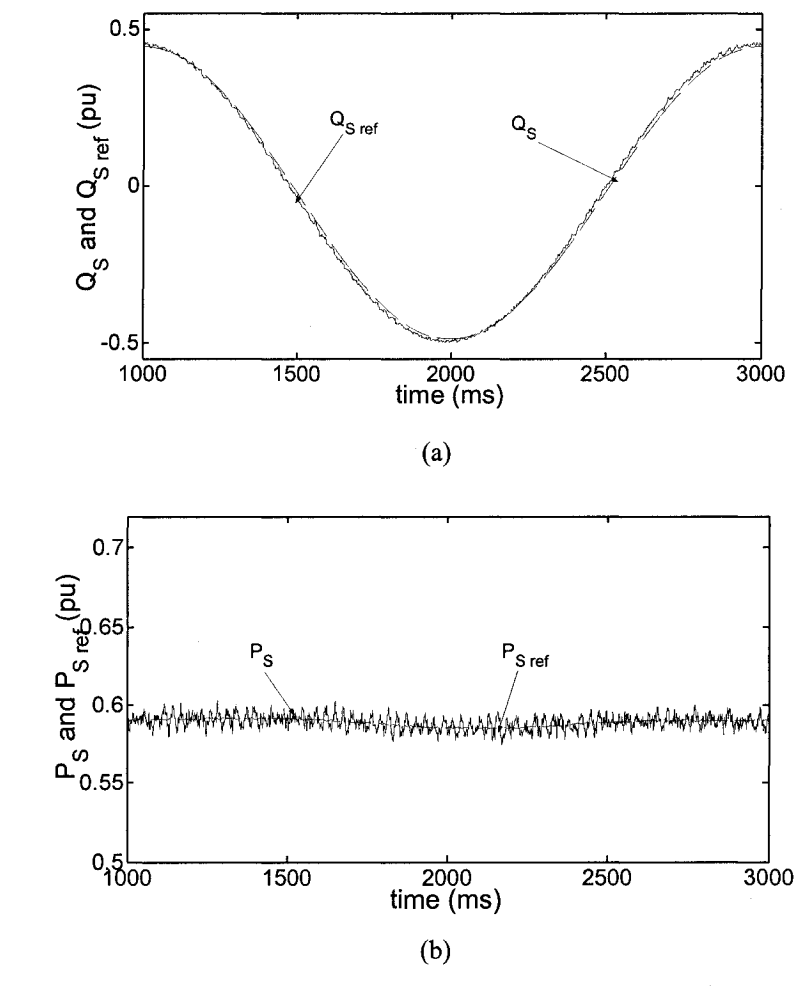


Fig. 4-13 Simulation of DFIG: Qs _{ref} variable, Ps _{ref}=constant When Rs=0
(a) Qs _{ref} and measured Qs
(b) Ps _{ref} and measured Ps

4.5.2.2 Stator Leakage Inductance Uncertainty-- L_{ls}

Fig.4-14 shows the simulations when the stator leakage inductance in the controls of Fig.4-4 is doubled the size of that of the DFIG in Appendix A, i.e L_{ls} =0.172 p.u. As Q_s and P_s almost coincide with their references Q_{sref} and P_{sref}, it is clear that the control is not sensitive to the parameter L_{ls} . The insensitivity comes from the fact that the magnetizing inductance is very large (L_m =3.10 p.u.) compared to the leakage inductance (L_{ls} =0.086 p.u.). Therefore, as $L_{ls}/L_m\approx0$, $L_S/L_m\approx1$ because $L_S=L_m+L_{ls}$. Thus (4.21) reduces to

$$\begin{pmatrix} i_{R\gamma}^* \\ i_{R\delta}^* \end{pmatrix} \approx \begin{pmatrix} i_{S\gamma}^* \\ i_{S\delta}^* \end{pmatrix} + \begin{pmatrix} 0 \\ -v_{S\gamma} / L_m \omega_S \end{pmatrix}$$
 (4.21.a)

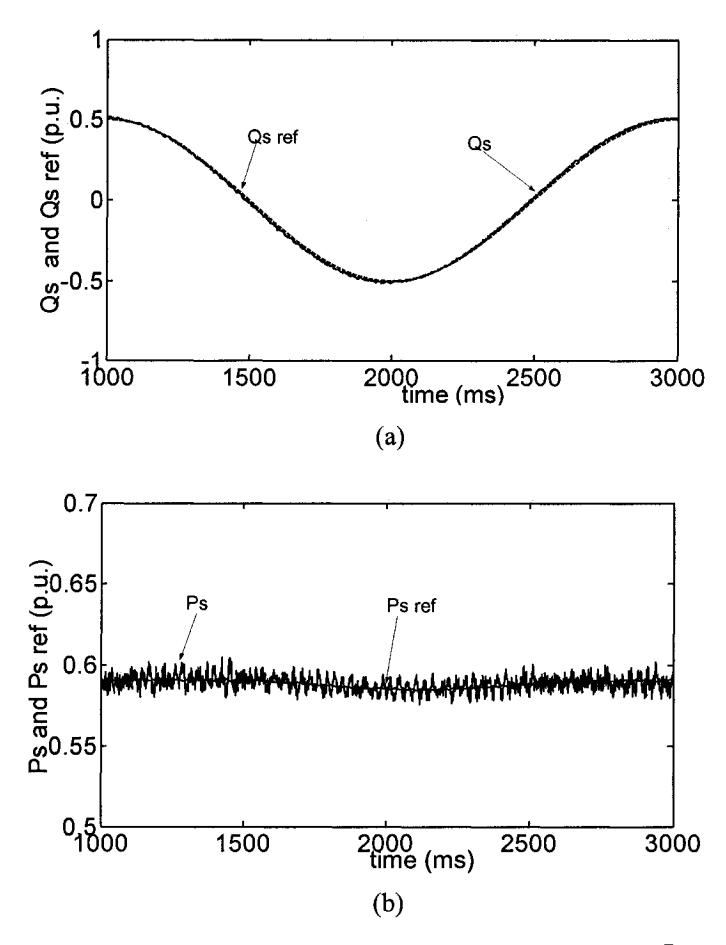


Fig. 4-14 Simulation of DFIG: Qs $_{\rm ref}$ variable, Ps $_{\rm ref}$ =constant When value of L_{ls} (0.172 p.u.) used in computation equals 2 times the actual value.

- (a) Qs ref and measured Qs
- (b) Ps ref and measured Ps

4.5.2.3 Magnetizing Inductance Uncertainty- L_m

The value of the magnetizing inductance of the DFIG in Appendix A is L_m =3.10 p.u. Simulations show that the decoupled P-Q control fails altogether when the magnetizing inductance in the control of Fig. 4-4 deviates beyond the following lower limit L_m <1.2 p.u. and beyond the upper limit L_m >5.6 p.u.

Fig. 4-15 shows the case when the magnetizing inductance used in Fig. 4-4 takes the value of L_m =1.55 p.u., which is half the value of the parameter of the DFIG in the simulation. Comparing the simulation of P_S in Fig.4-15 (b) with those in Fig. 4-13 (b) and 4-12 (b), one concludes that the sensorless decoupled P-Q control is more sensitive to L_m than to R_s and L_{ls} . Nevertheless there is coarse tracking. This is because $v_{S\gamma}/(L_m\omega_S)$ in

(4.21.a) a small magnetizing current. When the magnetizing current is sufficiently small, (4.21.a) reduces to another approximation:

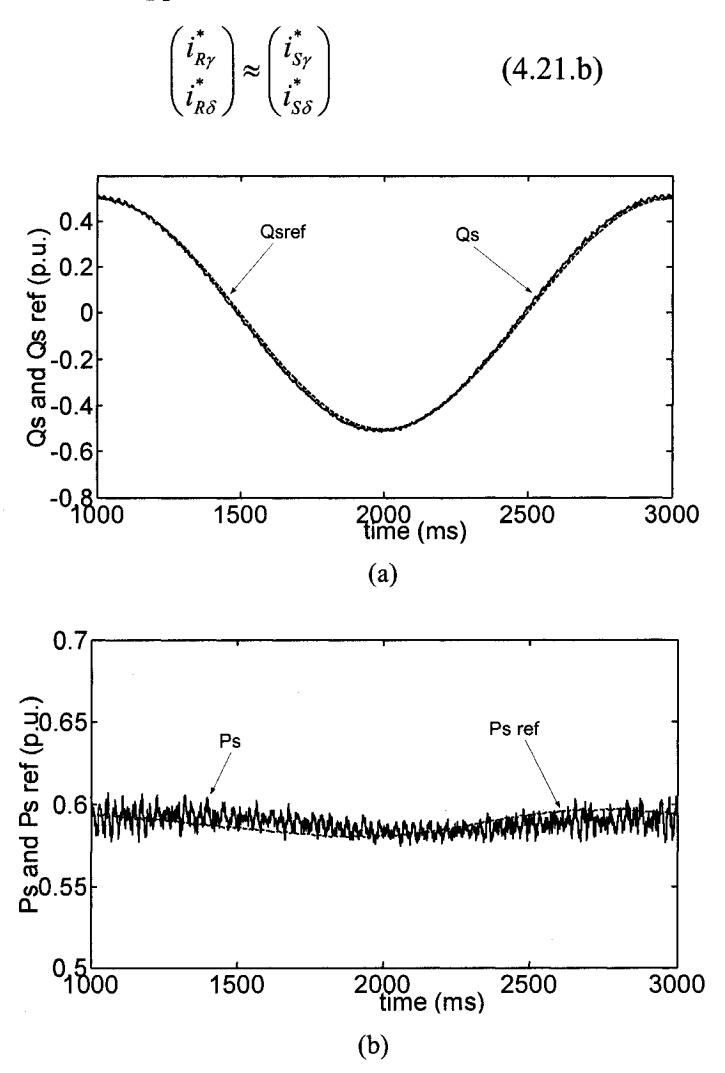


Fig. 4-15 Simulation of DFIG: Qs $_{\rm ref}$ variable, Ps $_{\rm ref}$ =constant When $L_m=1.55\,p.u.$ (a) Qs $_{\rm ref}$ and measured Qs (b) Ps $_{\rm ref}$ and measured Ps

4.5.2.4 Basis of Robustness

Because $(L_m \omega_S)$ is very much larger than R_s , $\omega_s L_{ls}$, R_R , $\omega_s L_{lR}$, the magnetizing reactance $(L_m \omega_S)$ is often approximated as an open circuit in the equivalent circuit of induction motor. In such an approximation, the rotor currents are taken as equal to the stator currents. This practice correspond to the approximation of (4.21.b) and for this

reason the robust control in Fig.4-4 has a solid theoretical base. The only requirement is that $(L_m \omega_s)$ is large. In general $(L_m \omega_s)$ can be easily and precisely measured.

4.5.3 Dynamic Tests

The dynamic tests planned for the control of Fig. 4-4 are in optimal wind power acquisition application. It is assumed that the wind turbine operates with a fixed pitch angle for which the wind power characteristics are as shown in Fig. 4-3. The control of Fig. 4-4 makes the rotor speed ω_m track the P_{max} -vs- ω_m curve as the wind velocity V_w changes.

As mentioned, two software black boxes, Fig.4-5 (a) and (b), have been developed to be used with the software DFIG of EMTP (R) and the control of Fig. 4-5 (b) represents the wind turbine. It has the wind velocity V_w and the rotor speed ω_m as inputs and the wind turbine torque T_{mech} as kits output. Fig.4-5 (a) represents the optimal wind power acquisition strategy. It has the rotor speed ω_m as its input and outputs the stator power reference P_s^* as its output.

4.5.3.1 Dynamic Test of Slip Frequency PLL and γ-δ Axes Aligner

Optimality in wind power acquisition has been proven by showing that the C_p of equ. (4.15) computed from the simulation results of the simulations, remains at the peak value in the C_p -vs- λ curve in Fig. 4-2. As the objective of this section of the chapter is to demonstrate that the decoupled P-Q control is robust, the results are presented to prove robustness only.

The simulation results in Fig. 4-16 are for the case in which the parameters entered in the control of Fig. 4-4 correspond exactly to the parameters of the DFIG in Appendix A. As a dynamic wind turbine problem, the wind velocity V_w is given a sinusoidal variation as shown in Fig. 4-16 (a). Fig. 4-16 (b) shows the rotor speed ω_m tracking the peak wind power corresponding to the wind velocity V_w . Fig. 4-16 (c) shows the stator power

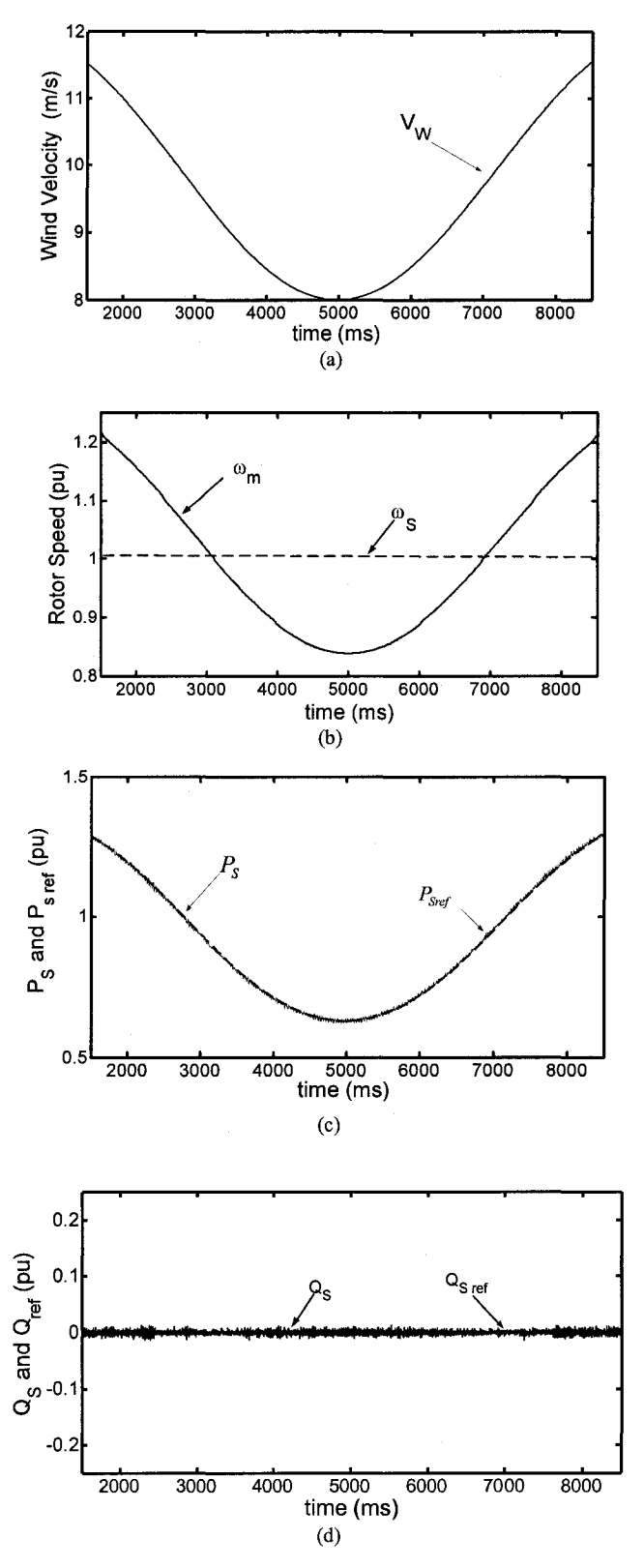


Fig.4-16 Simulation of DFIG in Optimal Wind Power Acquisition: Variable wind speed, Qs _{ref}=constant (a) Wind Velocity; (b) Rotor Speed; (c) Ps _{ref} and measured Ps; (c) Qs _{ref} and measured Qs.

reference P_{Sref} of the optimal wind power acquisition strategy. In this test, the reactive power reference Q_{Sref} is held constant.

The success of the control of Fig. 4-4 lies in the measurements P_S and Q_S overlapping their references P_{Sref} and Q_{Sref} . Also, the varying real power is not coupled to the reactive power.

4.5.3.2 Dynamic Test of Robustness

Fig. 4-17 repeats the previous test except for the change made to the parameters entered in the control blocks from the parameters entered in the DFIG software.

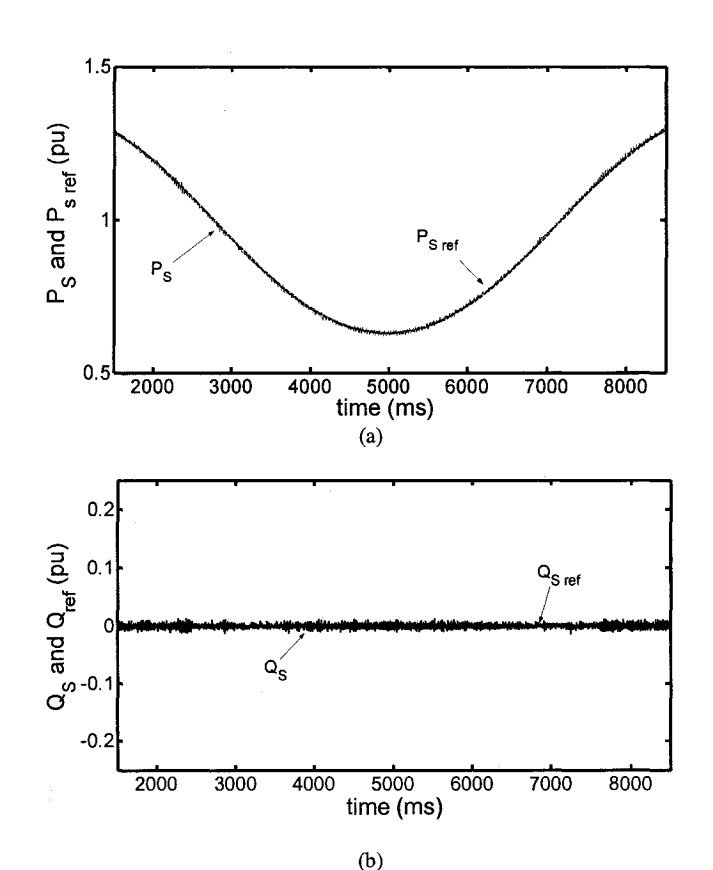


Fig.4-17 Simulation of DFIG in Optimal Wind Power Acquisition: Variable wind speed, Qs ref=constant when $R_s = 0$, $L_{ls} = 0$ and $L_m = 1.55 p.u$.

(a) Ps ref and measured Ps; (b) Qs ref and measured Qs.

In the control blocks the changes made are: $R_s=0$, $L_{ls}=0$ and $L_m=1.55$ p.u. Otherwise, the other parameters are the same as in Appendix A which are used in the DFIG. In spite of the significant parameter differences, Q_S tracks Q_{Sref} and P_S tracks P_{Sref} closely.

In general, one sees that robustness has been built into the control by the current tracking strategy.

4.6 CONCLUSION

In this chapter, the two novel sensorless means, the Slip Frequency PLL and the $\gamma - \delta$ Axes Aligner, have enabled decoupled P-Q control to be implemented at the rotor terminals of a DFIG. In simulation tests, the sensorless control has been applied to capture maximum wind power which is dependent on the wind velocity.

This chapter has shown that the decoupled P-Q control can be made robust by making the rotor-side Voltage-Source Converter function as current tracker. Simulation results show that the sensorless control is insensitive to parameter variations in R_S and L_{IS} . Tolerance to variation in the magnetization reactance L_m is restricted. However, this is not of great concern since this parameter can be precisely measured.

Chapter 5

Conclusions and Future Work

The primary objective of this thesis is to realize a new sensor-less, P-Q control strategy to a DFIG. As mentioned in the introduction in chapter 1, there already exists a sensor-less P-Q control strategy for the DFIG. The existing method is based on computing the instantaneous position of the γ - δ frame and the rotor position from the stator and rotor measurements of currents and voltages using the γ - δ frame equations of the induction machine. Then the rotor speed is obtained by differentiating the rotor position.

This thesis has proposed an alternate method. Because the ideas of this thesis have just been formulated and proven only by simulations, it is still too early to know how competitive the method is. The new sensor-less method relies on two components: (i) the Slip Frequency Phase Lock Loop (PLL) which locks on to the 3-phase rotor currents and establishes the rotor current γ^* - δ^* axes. The measurements available are: the rotor speed, the phase and the frequency of the rotor currents; (ii) the γ - δ Axes Aligner for aligning the rotor current γ^* - δ^* axes to locate the stator voltage γ - δ axes.

Slip Frequency PLL

The novel Slip frequency PLL is adapted from the conventional PLL. The innovative adaptation is required because the conventional PLL may not be able to handle with the positive slip frequency, the zero slip frequency and the negative slip frequency as the rotor passes from sub-synchronous speed to synchronous speed and then to super-synchronous speed. Simulation tests show that this Slip Frequency PLL tracks the rotor current phase and frequency without difficulty and has excellent transient response, even in the presence of large switching noise from the PWM switching of the rotor-side Voltage-Source Converter.

Furthermore, its attractiveness lies in the fact that one of the outputs of the Slip Frequency PLL is the estimated rotor speed. The speed is obtained *directly* and *not* by

differentiating the estimated position as in the method used in [6,8,9]. As differentiation is notoriously noisy and filtering of the noise incurs a phase lag, the Slip Frequency PLL is potentially more accurate than the method of [6,8,9].

Phase Lag in Estimated Speed

However before such a claim can be made, it is necessary to find out if the Slip Frequency PLL is itself free of phase lag. The frequency response of the Slip Frequency PLL has been measured and there is a phase lag which increases with the frequency of the mechanical perturbation on the rotor. To determine the source of the phase shift, the Slip Frequency PLL is analyzed in detail and the conclusion reached is that the phase shift does *not* come from the Slip Frequency PLL.

The next possible location for the source of the phase lag is the wound-rotor induction machine (DFIG) itself. The suspected culprit is the time delay between the currents and the speed induced rotor voltage which is related to the time constants $T_S = L_{IS}/R_S$ and $T_R = L_{IR}/R_R$ of the stator and rotor windings. This suspicion has been proven by simulations.

Phase Lag in Estimated Speed by Sensor-less Methods

Both methods, the method of [6,8,9] and the Slip Frequency PLL rely on current measurements in their sensor-less estimations and therefore this phase lag, associated with electrical time constants, is necessarily common to both methods. However, the Slip Frequency PLL does not have an additional delay from the filter required to remove noise of the differentiation operation, in deriving speed from rotor position.

The thesis has shown that, should it be necessary, the phase lag can be compensated by a Lead-Lag Transfer Function Block.

It should be remembered that the application of the sensor-less speed estimator is in a wind turbine-generator system where the mechanical time constant is very much larger than the electrical time constants. The improvement in accuracy is academic only and not likely to affect the overall performance of the DFIG.

However, the existence of such time delay as inherent in "sensor-less" measurement methods is important from the viewpoint of measurement theory.

γ-δ Axes Aligner

The Slip Frequency PLL is capable of setting up the γ^* - δ^* frame of the rotor *currents* which rotates synchronously at ω_S , the same speed as the γ - δ frame of the stator *voltages*. For decoupled P-Q control, it is the γ - δ frame of the stator *voltages* which must be located and since the γ^* - δ^* frame of the rotor currents is available it is a matter of phase shifting it until the voltage of the stator δ -axis $\nu_{S\delta}$ =0. The Axes Aligner is based on a negative feedback loop which rotates the γ^* - δ^* frame until $\nu_{S\delta}$ =0. (Equivalently, the negative feedback loop rotates the γ^* - δ^* frame around until $\nu_{S\gamma}$ reaches the predetermined value for which $\nu_{S\delta}$ =0.) Once, the γ^* - δ^* frame is aligned, it becomes possible to implement decoupled P-Q control.

Robust Sensor-less Decoupled P-Q Control of DFIG

The work of this thesis has followed in the footsteps of [9,10]. As these publications have given the impression that all the parameters of the DFIG must be known before in Sensor-less Decoupled P-Q Control of a DFIG can be successfully implemented, the challenge is to find a robust method, which is not dependent on knowing the parameters accurately.

The thesis has shown by analysis that by applying rotor current tracking control, Decoupled P-Q Control of DFIG can be implemented even when the parameters (such as the magnetizing inductance, the rotor winding resistance and leakage inductance) are known imprecisely. The robustness, predicted by the analysis, has been substantiated by simulations.

Optimal Wind Power Acquisition by Robust Sensor-less Decoupled P-Q Control of DFIG

The thesis has successfully simulated Robust Sensor-less Decoupled P-Q Control as part of a wind-turbine driven doubly-fed induction generator (DFIG) in a situation where the wind velocity is given a sinusoidal fluctuation in time. The wind-turbine dynamics is modeled by a software block which accepts the wind-velocity and the wind-

turbine speed as inputs and which outputs the corresponding wind torque as output. The Optimal Wind Power Acquisition strategy is programmed in a Lookup Table which is addressed by the wind-turbine speed and which outputs the stator power of the DFIG,

 P_{s-ref} to the Decoupled P-Q Controller. The successful simulation of this dynamical test has established further credibility of:

- (i) the Slip Frequency PLL and the γ - δ Axes Aligner as robust sensor-less methods
- (ii) the rotor current tracking control as the means to achieve robustness in Decoupled P-Q Control doubly-fed induction generator (DFIG)

Suggestions for Future Work

- (i) The simulation research of this thesis needs experimental substantiation.
- (ii) It should be possible for the Slip Frequency PLL and the γ - δ Axes Aligner to be compacted into a single unit. This is because both the Slip Frequency PLL and the γ - δ Axes Aligner track phase angles. The Slip Frequency PLL tracks the rotor current a-phase. The γ - δ Axes Aligner tracks the stator voltage a-phase.
- (iii) The system of the thesis should be tested under severe fault conditions.

REFERENCES

- [1] www.eia.doe.gov/oiaf/kyoto/kyotorp.html
- [2] Windenergie (2001), Available: http://www.wind-energie.de/informationen
- [3] P.C. Putnam, "Power from the wind", 1984, Van Nostrand Reinhold CO., New York USA, ISBN 0-13-960527-4
- [4] Weixing Lu and Boon Teck Ooi, "Multi-Terminal LVDC System for Optimal Acquisition of Power in Wind-Farm Using Induction Generators," Power Electronics Specialists' Conference, June 2001, Vancouver
- [5] B.T.Ooi and X.Wang, "Boost type PWM-HVDC transmission system", *IEEE Transactions on Power Delivery*, Vol. 6, No.4, October 1991, pp. 1557-1563
- [6] L.Xu and W. Cheng, "Torque and reactive power control of a doubly fed induction machine by position sensorless scheme", IEEE Trans.Ind. Applicant., vol.31 pp.636-642, May/june 1995
- [7] R.Pena, J.C.Clare, and G.M Asher, "Doubly fed induction generator using back-to-back PWM converters and its application to variable-speed wind-energy generation" Proc. Inst. Elect. Eng., pt. B, vol.143 no.3, pp.231-241, May 1996
- [8] L.Morel, H.Godfroid, A.Miraian, and J.M. Kauffmann, "Doubly-fed induction Machine: converter optimization and field oriented control without position sensor", Proc. Inst. Elect. Eng., Pt.B. vol.145, no.4 pp.360-368 July 1998
- [9] R.Datta and V.T. Ranganathan, "A simple Position-sensorless Algorithm for Rotor-side Field-Oriental control of Wound-Rotor Induction Machine", IEEE Trans. Ind. Elect., vol.48,No.4, August 2001
- [10] Hirofumi Akagi and Hikaru Sato, "control and performance of a Doubly-fed Induction Machine intended for a flywheel energy storage system", IEEE Trans. On Power Elect., vol.17, No.1, January 2002
- [11] Jian Hu, "Deadbeat Controlled PWM Converter", Thesis of department of electrical engineering, McGill University. Montreal, 1999, Canada
- [12] Baike Shen, Victor Low, B.T. Ooi, "Slip Frequency Phase Lock Loop (PLL) for Decoupled P-Q Control of Doubly-Fed Induction Generator (DFIG)", The 30th Annual Conference of the IEEE Industrial Electronics Society, Nov.2004

- [13] Charles L Philips, H. Troy Nagle, "Digital Controlled Systems, Analysis and Design", Prentice Hall 1990
- [14] Pierre R. Belanger, "Control Engineering, A modern Approach", Saunders College Publishing 1995
- [15] Lianwei Jiao, Geza Joos, Chad Abbey, Fengquan Zhou, B.T. Ooi, "Multi-Terminal DC (MTDC) System for Wind Farms Powered by Doubly-fed Induction Generators (DFIGs)", IEEE Power Electronics Specialists Conference, PESC04, Achen, Germany, 2004
- [16] Chee-mun Ong, "Dynamic Simulation of Electric Machinery using Matlab/Simulink", 1998, Prentice Hall Upper Saddle River, NJ 07458, ISBN 0-13-723785-5
- [17] Burton T., D. Sharpe, N. Jenkins, and E.Bossanyi, "Wind Energy Handbook". New York, J.Wiley, 2001
- [18] Y.H.A. Rahim, "Controlled Power Transfer from Wind Diven Reluctance Generator", IEEE Trans. On Energy Conversion, vol. 12, No.4, December 1997
- [19] Juan W.Dixon, B.T. Ooi, "Indirect Current Control of a Unity Power Factor Sinusoidal Current Boost Type Three-Phase Rectifier", IEEE Transactions On Industrial Electronics, vol.35,No.4, November 1998
- [20] B.T. Ooi, Notes of course ECSE-565A, "Introduction to Power Electronics", in McGill University (2002)
- [21] Chad Abbey, Geza Joos, "A Doubly-fed Induction Machine and Energy Storage System for Wind Power Generation", CCECE 2004-CCGEI 2004, Niagra Falls, May.2004 0-7803-8253-6/04

Appendix A

The Schematic of the circuit used in the EMTP(R) simulation is shown in Fig.A.1

The simulation step is 5 microsecond.

The parameters of the Doubly-fed Induction Generator in Fig.A.1 are:

Rated Power 1MVA

Stator 3.3 kV

Stator/Rotor Turns Ratio 1:1

Frequency 60Hz

R_S=0.00662 p.u.

 $L_m=3.1$ p.u.

 L_S =3.185 p.u.

 L_R =3.21 p.u.

 $R_R = 0.01$ p.u.

 $Z_{base} = 10.98 \Omega$

76

